RSC
Applied Interfaces

ROYAL SOCIETY OF CHEMISTRY

REVIEW

View Article Online
View Journal



Cite this: DOI: 10.1039/d5lf00380f

# Sensor and protection technologies against viruses using porphyrin-based MOFs and COFs

Pierre D. Harvey

Received 3rd December 2025,
Accepted 22nd February 2026

DOI: 10.1039/d5lf00380f

rsc.li/RSCApplInter

Since the COVID-19 pandemic began in 2020, there has been a surge of interest in detecting, controlling and eradicating viruses, and developing technologies accordingly. The colored, strongly luminescent, and photo- and electrochemically active porphyrin-based metal–organic frameworks (MOFs) and covalent-organic frameworks (COFs) were also explored over the past decade. This review covers significant research developments for efficient viral detection, protection and elimination that occurred mostly during the past decade. Sensor designs utilise porphyrin-based MOFs and COFs as interfaces to selectively detect biological materials associated with target viruses (for example, the capture of RNA as a stimulus) with very high sensitivity, thus allowing for the early diagnosis of their associated diseases. The sensor techniques are based on chemiluminescence, electrochemiluminescence, photoelectrochemical bioassays, and the photodynamic effect. The deactivation of viruses is based on the photodynamic therapy approach, where the photosensitization of singlet oxygen is performed by the porphyrin chromophore, which is unavoidably placed in close proximity to the virus due to the short-lived reactive oxygen species (ROS; 3.1 μs in water). The characteristics of this ROS entity and the underlying mechanism are described with some relevant details. Finally, the development of self-protection is also addressed in the literature, which concerns the modification of face masks with porphyrin-based porous materials for adsorption purposes.



## Introduction

Many viruses such as dengue, Ebola, influenza, hepatitis, rabies, varicella, and Zika viruses, human immunodeficiency virus (HIV), polioviruses and coronaviruses remain a major societal health concern. The huge demand for antiviral solutions has pushed scientists to explore the use of nanomaterials, particularly MOFs and COFs, to assess their usefulness and efficacy in sensing these harmful infectious agents, preventing their entry into the human body or isolating them, and deactivating them either through direct contact with these nanosized entities or through photosensitization to generate ROS, notably singlet oxygen ($^1O_2$). Indeed, over the past decade, the number of research articles has increased steadily (Fig. 1), but this field is unambiguously still in its infancy. A review article on the development of new technologies dealing with viruses *versus* MOFs has been recently published, and the first general observation was that there are six basic approaches developed to manage viruses using these nano-devices. This series can be divided into two main categories: virus isolations and eliminations.[1] The former is subdivided into three strategies: (a) encapsulation inside a MOF cavity, (b) placement of a physical barrier of some sort to prevent contact with humans, and (c) mineralisation (with MOFs) around the virus. The second category is also divided into three methods: (d) delivery of antiviral drugs, (e) design of antiviral MOFs, and (f) sanitization by the photosensitization of dioxygen into $^1O_2$.

*Département de Chimie, Université de Sherbrooke, 2500 Boul. de l'Université, Sherbrooke (QC), J1K 2R1, Canada. E-mail: Pierre.Harvey@USherbrooke.ca*

**Pierre D. Harvey**

*Prof. Harvey obtained his PhD from McGill University (1986) and pursued his postdoctoral studies at the California Institute of Technology (1986–88) and the Massachusetts Institute of Technology (1988), before moving to the Université de Sherbrooke as an assistant professor (1989). He held a Chaire d'Excellence de Recherche from the ANR (Dijon, France, 2008–2010) and received many prizes, including the Rio Tinto Alcan Award from the Canadian Society of Chemistry (2013). He published over 370 peer-reviewed articles and 8 book chapters. His research focuses on the photochemistry and electrochemistry of coordination materials, including porphyrin-based metal–organic frameworks and the chemical design of solar cell components.*

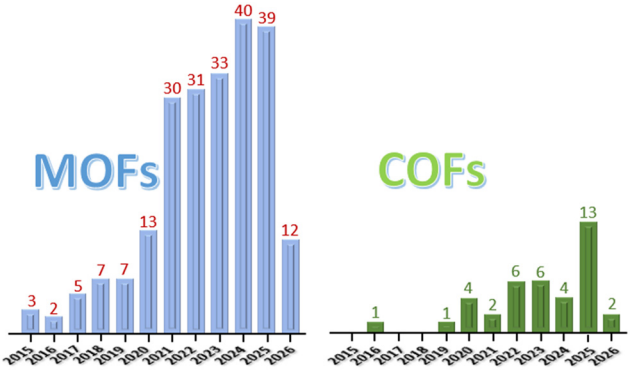


**Fig. 1** Graphs reporting the number of research articles devoted to describing new applications of metal–organic frameworks and covalent-organic frameworks for virus management since 2015 based on a recent library search using the SciFinder engine (2026-02-18). Patents, reports, preprints, and conferences are not included.

The second take-away message is that, except for rare investigations on the detection of some viruses, porphyrin-based MOF technologies were not fully developed for these purposes. This observation is quite surprising since the stand-alone porphyrin dyes and their derivatives are well-known to serve the last task: virus elimination by the photosensitization of dioxygen into $^1O_2$.[2–7] The porphyrin dye and its derivatives have the advantage of being colored, and under sunlight or room light, these pigments absorb visible light and perform this very basic yet important photophysical activity, potentially leading to sustainable developments. The third key information conveyed is that the porphyrin-based MOFs, essentially PCN-222 and PCN-224 (PCN = porous coordination network; Fig. 2), are the most employed interfaces.[8] PCN-223 is also a common porphyrin-based MOF, but it is used to a much lesser extent. PCN-222 and PCN-224 were tested for their cytotoxicity against J774A.1 cells using the Neutral Red assay method (Fig. 3).[9] The cytotoxic concentration was found to be greater than 10 to 20 nM.

Since this last review,[1] the use of colored, emissive and redox-active porphyrin-based MOFs and COFs has made a significant progress. This mini review covers these recent developments where three approaches are exploited: detection using various analytical techniques, prevention of contact with humans, and elimination by antimicrobial photodynamic therapy.

## Section 1. Evolution of various stand-alone porphyrin-based antiviral technologies

### The early days

To the best of our knowledge, the concept of porphyrin-based remedy to pathogenic substances, including viruses, as photosensitizers appeared in 1934 (SciFinder).[10] This technique has become more standardized afterward, where solutions containing various viruses with porphyrins were irradiated with daylight, but different efficiencies were observed depending on the viruses.[11] In a similar manner, the control of plant viruses was also addressed using *in vitro* methods by simple contacts between porphyrins and the plant-related viruses, but it was unclear

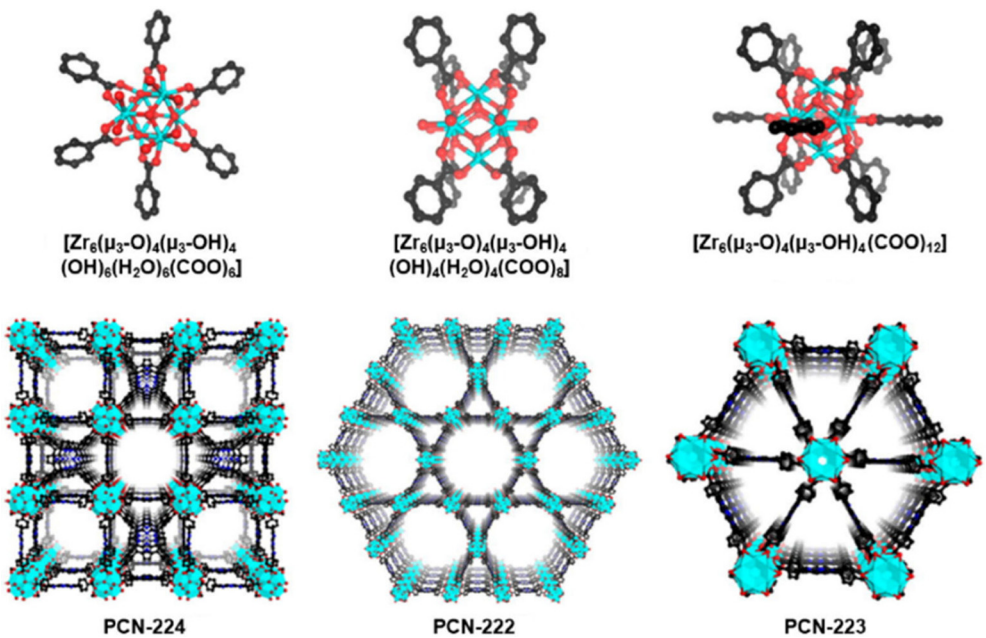


**Fig. 2** Illustrations of the 3D-porphyrin-based MOF structures of PCN-222, PCN-223, and PCN-224 built with the ligand TCPP (5,10,15,20-tetrakis(carboxyphenylporphyrin)) and various zirconium(IV) compounds such as $ZrOCl_2$ and $ZrCl_4$. These MOFs are the most used in the area of antimicrobial photodynamic therapy and the detection of pathogens. Reproduced with permission from ref. 8. Copyright 2020 Elsevier.

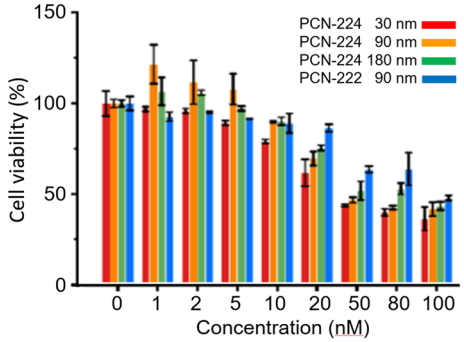


Fig. 3 Viability of J774A.1 cells treated with different concentrations of PCN-224 and PCN-222 for 24 h. Reproduced with permission from ref. 9. Copyright 2022 Elsevier.

whether the samples were exposed to day light or not, and the amount of materials used was large (300 ppm; 1 ppm = 1 mg $L^{-1}$).[12] Concurrently, applications in the medical field through photodynamic inactivation of viruses, such as Moloney mouse leukemia virus,[13] herpes simplex virus types 1 and 2,[14–17] influenza A,[16] Phage T4,[18] and vaccinia virus,[19] using visible light started to emerge in the late 1970s and 1980s. The approach of photodynamic inactivation of viruses is still employed today, but the focus may vary between targeting the virus as a whole and specifically targeting its RNA.

A turning point in the early 1980s is the emergence of AIDS (acquired immunodeficiency syndrome) caused by HIV-1 (human immunodeficiency virus) as a pandemic. This event triggered a large interest in finding solutions to this disease (Fig. 4), including using the photodynamic inactivation properties of porphyrin species,[20,21] or testing their $IC_{50}$ (inhibitory concentration 50%) efficacy,[22,23] or both.[24] Concurrently, other viruses were also subjects of investigations, for instance feline leukemia virus,[25,26] vesicular stomatitis virus,[26] Epstein–Barr virus,[27] and Friend leukemia viruses.[28] In a similar manner, the COVID-19 pandemic started in 2019, and was caused by the severe acute respiratory syndrome coronavirus 2 (SARS-CoV-2), and rapidly the first investigation on the photoinactivation of this coronavirus appeared just 2 years after this date.[29]

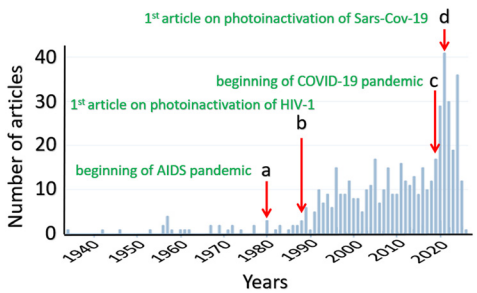


Fig. 4 Graphs reporting the number of research articles containing the key words "porphyrin" and "virus" from a recent library search using the SciFinder engine (2026-02-18). Patents, reports, preprints, metal–organic framework, MOF, and conferences are not included.

**Nowadays**

Essentially, the number of studies focusing on the photoinactivation of viruses, in general, has increased where the scope of viruses was enlarged significantly. The inactivation methods (under irradiation or by contact) of viruses and other pathogens by porphyrin dyes and their derivatives have also been the subject of recent reviews.[30–33] It is also noteworthy that the use of stand-alone porphyrin derivatives for the detection of viruses has not been explored very much.

## Section 2. Development of sensors

Sensor technologies using porphyrin-based MOFs and COFs as components in nanosized detection devices have only recently emerged. One of the obvious and interesting traits of porphyrin-based MOFs and COFs is the possibility to exploit their often-encountered intense fluorescence as shown below.[34] However, these porous materials can also act as platforms. For instance, porous 2D sheets of porphyrin-based MOFs as nanosized platforms can be used for the detection of DNA.[35] In this study, 2D-MOFs were prepared exploiting the strong chelating properties of the *tert*-pyridyl ligand with $MCl_2$ salts (M = $Co^{2+}$, $Ni^{2+}$, and $Fe^{2+}$) using the Langmuir–Blodgett method (pressing speed of 35 mm $min^{-1}$) and layer-by-layer transfer on a substrate (Fig. 5). The Q-band signature (4 bands) confirmed the absence of metal inside the macrocycle.

In this technique, slight excess of Texas red-labeled ssDNA probe ($\lambda_{emi}$ = 615 nm; $\lambda_{exc}$ = 585 nm; denoted as **Probe**) was hybridized with target ssDNA (**Target**), forming a solution containing both emissive ssDNA **Probe** and dsDNA **Probe**/**Target** species. When exposed to the (photoconducting) quartz-assisted 2D-$[Co\text{-}TTPP]_n$ nanoplatform, the excess of ssDNA **P1** binds with the 2D-layers through electrostatic interactions, and perhaps H-bonds with the chloride ions, inside the cavities made by the wide square structure of the 2D sheets. This proximity between the chromophores provokes the fluorescence quenching of **Probe** by electron transfer. Using different excess of **Probe**, the residual fluorescence intensity of dsDNA **Probe**/**Target** species allows for an accurate assessment of the quantity of DNA present in solution in the linear ranges of 0–20 nM down to the 0–1 nM range. When M = $Co^{2+}$ (best of the three transition metal ions investigated), a limit of detection of 120 × $10^{-12}$ M was reported. This "classic" biological approach can also be extrapolated to RNA, which is isolated from viruses. Therefore, the main approach for the detection of viruses is largely based on provoking a response where RNA plays a major role in causing a change in the biological environment of the sensor. These techniques are electrochemiluminescence, chemiluminescence, photoelectrochemical bio-assays, and photodynamic effect, implying that the detection signals are luminescence, electric current, and occurrence of a chemical reaction.

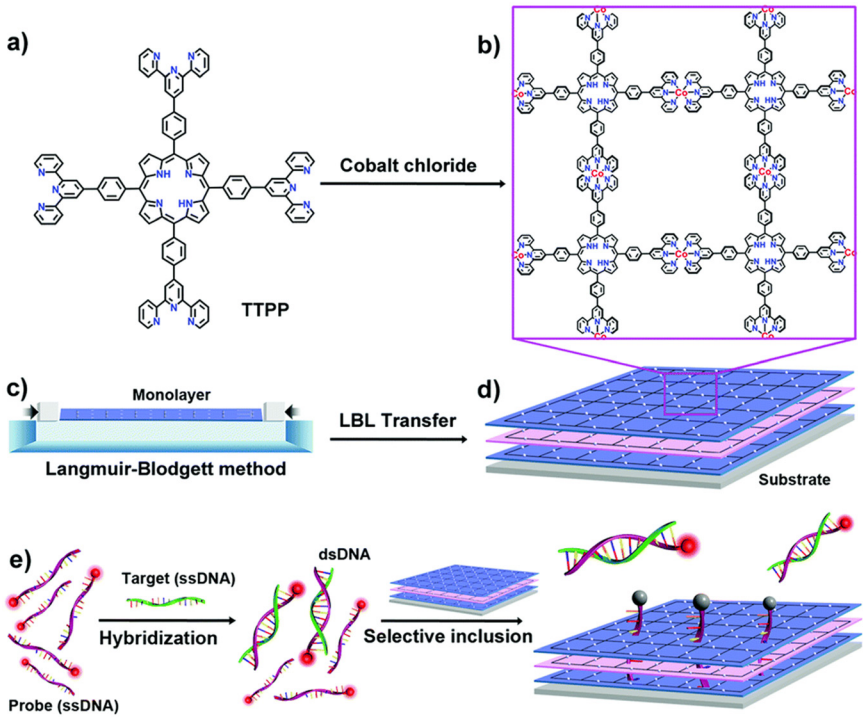


**Fig. 5** Illustration showing the preparation of the porphyrin-based MOF nanoplatforms. a) Structure of the tetradentate TTPP ligand. b) Structure of 2D-[Co-TTPP]$_n$; $Cl^-$ ions are not shown. c) Scheme representing the Langmuir–Blodgett device preparing a monolayer of 2D-[Co-TTPP]$_n$ at the air/liquid interface. d) Overall schematic showing the controllable layer-by-layer (**LBL**) transfer of 2D-[Co-TTPP]$_n$. e) Fluorescence DNA detection by the quartz-assisted 2D-[Co-TTPP]$_n$ nanodevice. Reproduced with permission from ref. 35. Copyright, the Royal Society of Chemistry 2019.

### 2.1 Sensors based on electrochemiluminescence responses

The porcine epidemic diarrhea virus, PEDV, causes vomiting, diarrhea and dehydration upon infection.[36] A technique based on electrochemiluminescence (ECL) has been recently developed by Han and collaborators to detect this virus,[37] which exhibits the advantages of high sensitivity (limit of detection = 0.4 pg mL$^{-1}$), low noise, and simple detection.[38] The key ingredient here is the porphyrin chromophore, which is conveniently electroactive and fluorescent, for ECL response. PCN-224 (Fig. 2; left) is among the porphyrin-based MOFs that have been used to detect pesticides and toxins related to agriculture using colorimetry, fluorescence, HPLC, and electrochemical and immunochromatographic methods, which exhibits high stability.[39] Concurrently, nanosized $TiO_2$ (rutile-structured) is often used in ECL devices, as it forms stable films and exhibits low toxicity.[40]

This ECL device for the detection of PEDV is constructed as illustrated in Fig. 6. First, PCN-224 is prepared ($H_2$TCPP plus zirconium(IV) salt/DMF and benzoic acid) under

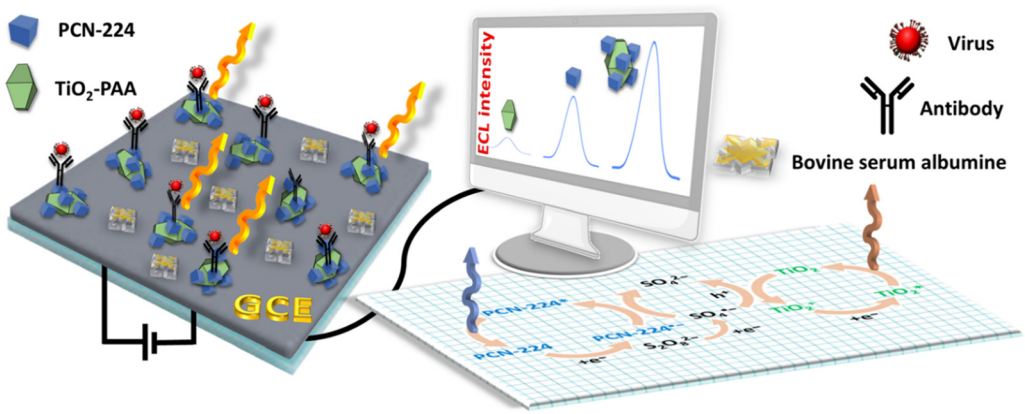


**Fig. 6** Drawing of the ELC device, surface components, and mechanism of the ELC signal when the device is in contact with the virus based on ref. 37. GCE = glassy carbon electrode.

solvothermal conditions, and its stability was verified in the presence of a potassium persulfate solution ($K_2S_2O_8$), and was fully characterized (TEM image, UV-vis and IR spectra, and $N_2$ BET isotherms at 77 K; pore size = 2.8 Å). Concurrently, $TiO_2$ NPs were wrapped into polyacrylic acid (PAA) to form the $TiO_2$-PAA composite, whereas the emissive and photoelectron-active PCN-224 was conjugated with a PEDV antibody, $Ab_1$, through amide-carboxyl bonds. The ECL device was constructed this way: $TiO_2$-PAA composite was deposited on a glassy carbon electrode (cathode operating between 0 and −1.2 V), followed by unconjugated PCN-224, and then conjugated with the PEDV antibody ($Ab_1$). Bovine serum albumin was also used among other proteins to verify that no interference occurs. The ECL signal was dependent on the surface (GCE) composition: $TiO_2$ < BSA/$Ab_1$/PCN-224/$TiO_2$ < $Ab_1$/PCN-224/$TiO_2$ < PCN-224/$TiO_2$. The virus is recognized and captured by the antibody $Ab_1$ thus provoking an ECL quenching by electron-transfer. This process interferes with the overall ECL mechanism (Fig. 5) aided by the short distance between the device components and the virus. A reproducible and stable linear relationship (10 cycles, with a relative standard deviation of 1.5%) between the ECL intensity and log[virus] was obtained, allowing the determination of a linear response range from 1 pg $mL^{-1}$ to 10 ng $mL^{-1}$ and a limit of detection of 0.4 pg $mL^{-1}$. When the device is stored one week in the fridge at 4 °C, the signal kept 94.2% of its original signal intensity. Swine faeces were used and adopted as real samples after testing. This study represents the first application of ECL by a porphyrin-based MOF for detection purposes.

Later, a new ECL biosensing device was fabricated by Jie, Zhou and collaborators for the detection of human papillomavirus type 16 (HPV-16),[41] which causes cervical cancer in woman. The ECL redox mechanism is the same as illustrated in Fig. 6, except that ZnO is used instead of $TiO_2$. It turns out that ZnO accelerates the reduction of $K_2S_2O_8$. The device was constructed using a gold electrode which was modified with a mixture of polyacrylamide (PAM). The latter provided a matrix forming stable and good quality films to accomodate zinc oxide NPs (n-type semiconductor). Then, through electrostatic attractions, the assemble was combined with nanosized PCN-224 particles (~500 nm, SEM) thus forming the sought nanocomposite (Fig. 7). The added gold NPs (~13 nm, TEM) bind hairpin shaped DNAs, which were then added to the surface of the device. After sealing the electrode with MCH, solutions of DNA S1 (GGATACGCACGACTCTAG) and 20 U of EXO III (exonuclease-based cycling cleavage) were successively added. The cycling cleavage process amplified tremendously the number of binding sites on the surface. Upon adding the target HPV-16 (HP1, HP2, and HP3; see Fig. 7 and its caption for details), binding and quenching occur. The limit of detection is 0.13 fM, and the linear range of response is 1 fM to 1 nM in the graph of ΔECL *versus* log[conc].

### 2.2 Sensors based on optical response chemiluminescence

Chemiluminescence is also a technique that has been exploited to design sensors for virus-related entities using porphyrin-based MOFs. In a recent investigation, Wang *et al.* targeted the Epstein–Barr virus (EBV) sometimes called herpesvirus 4.[42] This virus is known to infect about 90% of the population worldwide.[43] When infected, the patient may not show symptoms, but sometimes it can lead to mononucleosis in children and young adults, and in other cases, it can lead to nasopharyngeal carcinoma (NPC). EBV-related antibodies are produced during infection and can be

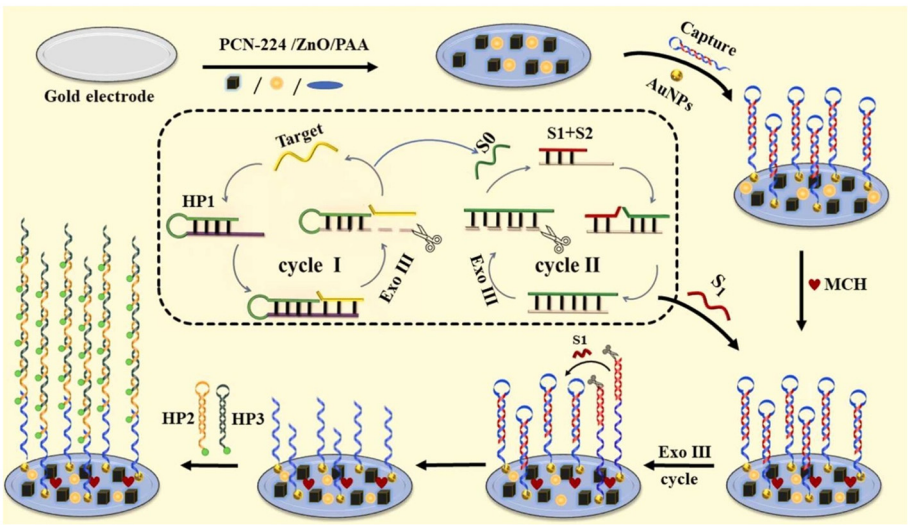


**Fig. 7** Illustration showing the construction of the ECL biosensing device using PCN-224/ZnO nanocomposites, along with the biological recognition materials and procedure (with cyclic amplification and chain reaction) for the detection of HPV-16. Reproduced with permission from ref. 41. Note: HP1 = GGACTGGATACGCACGACCTAGTTTTTCTAGGTCGTGCGTATC CAGTCCATCTCTACTGTTATGAG; HP2 = GGCACCATCGATGA GTCGTGCCGTGGGCTGATC, and HP3 = GACTCATCGATGGTGCCGAGGGATCAGCCCACG.

employed for early detection.[44] These antibodies include early antigen (EA-IgA), nuclear antigen (NA-IgA) and virus capsid antigen (VCA-IgA), and can be found in high levels in blood. An early screening for NPC patients, where EBV-IgA are in low quantities, is necessary. Moreover, targeting the three antibodies increases the accuracy of the diagnosis. The concept and procedure outlined by Wang *et al.* are illustrated in Fig. 8.

Briefly, the nanosized porphyrin-based MOF (MOF-FeP), for which the building blocks are TCPP(FeCl) and Zr(IV), was first prepared and then fully characterized (SEM, TEM, PXRD, XPS, EDS, and UV-vis spectroscopy). The size was just slightly smaller than 100 nm. It was first post-functionalized with COOH-PEG-NHS and then conjugated with a mouse anti-human IgA antibody (MOF-FeP@anti-human IgA), which was used to detect EBV-IgA. Three test lines of EA-IgA, NA-IgA and VCA-IgA (red triangles) were created on a hospital strip, along with a control line of anti-mouse IgG antibodies. Blood samples from NPC patients were collected and prepared for analysis. The composite MOF-FeP@anti-human IgA is placed at the beginning of the pad. When the EBV-IgA in the blood samples migrates throughout the pad, it binds with the composite MOF-FeP@anti-human IgA (recognition step) and continues to migrate with the flow (chromatography) until it reaches the three test lines where another recognition step occurs through binding with the EBV-antigens. With time, accumulation occurs inducing an amplification step. In the situation, there is no EBV-IgA in the blood samples, thus only the control line accumulates the composite. The control shows that migration did indeed occur, but the sample did not contain any EBV-IgA, meaning the blood does not contain evidence of virus infection. At high concentrations of EBV-IgA, the hospital strip can simply be used as a colorimetric sensor based on the photographs provided. However, for early detection, another approach is needed. To induce chemiluminescence, luminol is injected; upon contact with the TCPP(FeCl) unit, it induces an oxidoreduction reaction with these entities, similar to peroxidase (*i.e.* catalytic decomposition of $H_2O_2$ induced by TCPP(FeCl)), and emission is observed. With blood dilutions between 1 : 20 000 and 1 : 10 000, chemiluminescence is observed. Serum samples were also analyzed using this method, which proved successful and showed superior sensitivity to traditional ELISA kits. On the whole, the porphyrin-based MOF, namely through the central iron(III) ion of the porphyrin macrocycle, was employed as a catalyst to stimulate another reaction, leading to an observable signal. The porosity of the MOF can be beneficial for capturing luminol through its pores, thus rendering the distance between TCPP(FeCl) and luminol much shorter, leading to a rapid and efficient response. However, this aspect was not addressed in this investigation.

It is also worth noting that the same main authors used the properties of similar porphyrin-based MOFs, labelled **MxP**, where x stands for Ir, Ru, Pt, and Pd, to induce peroxidase-like activity, with the goal to cure NPC patients.[45] It turns out that the iridium-based MOF was the most efficient. The strategy involves post-functionalizing these **MxP** with epigallocatechin-3-gallate ligands, which detect the EBV associated with this disease. Then, $H_2O_2$ is catalytically and efficiently decomposed in hydroxy radicals by these porphyrin-based MOFs, thus causing severe damages to the surrounding cells where the EBVs are located.

### 2.3 Sensors based on the photodynamic effect

This methodology uses the photosensitization of singlet oxygen, $^1O_2(^1\Delta_g)$, by the porphyrin unit within the MOF in an assembly, which in turn oxidises a well-known indicator efficiently, thus providing a quantifiable signal intensity change. A necessary description of $^1O_2(^1\Delta_g)$, its *in situ* preparation, properties, and applications are provided in a section below. In this section on photodynamic effect, SARS-CoV-2 is addressed. Patients with COVID-19 suffer from acute respiratory distress syndrome (ARDS) caused by the down- or upregulation of the mechanism for the binding of porphyrin to iron in heme during its formation (meaning the iron

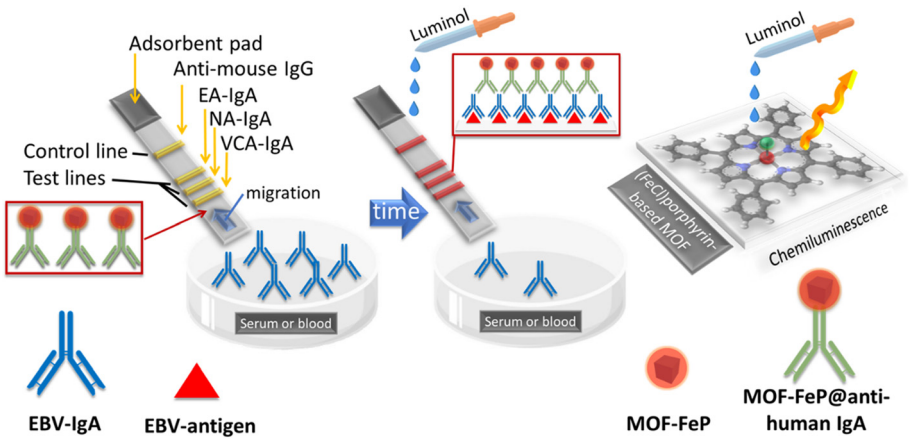


Fig. 8 Schematic of the biological strip, surface components and reactants, and the mechanism for the chemiluminescence response of luminol when EBV-IgA is in contact with the biological surface components according to ref. 42.

atom is not placed inside the macrocycle), and interference with the immune system leading to severe consequences.[46] For early detection, the selective recognition of its RNA can be performed with complementary oligonucleotide sequences; single-strand DNAs (ssDNA), for example. In this recent study, Zhu and his collaborators designed a rigorous methodology to address this need using a porphyrin-based MOF knowing that it can be easy to post-functionalize and photosensitize $^1O_2(^1D_g)$ efficiently (Fig. 9).[47] Several preliminary steps are necessary, including viral lysis (isolation of the **target RNA**), preparation of the MOF@DNA1 composite, and preparation of silica-decorated magnetite nanoparticles, FSN NPs ($Fe_3O_4$@$SiO_2$-$NH_2$), and those post-functionalized with DNA2 (FSN@DNA2 composite). The nanosized MOF (PCN-224) was synthesized and post-functionalized with DNA1 (**TTGAAGAGGACGATCT TACCGACCGT**), and the nanosized FSN was functionalized with DNA2 (COOH-*AGCAGCATCACCGCCAT*), both of which bind **AACUUCUCCUGCUAGAAUGGCUGGCA***AUGGCGGUGAU GCUGCU* (*i.e.* **target RNA**). Note that the bold and italic text indicate the complementary strands that bind to each other. Finally, FSN@DNA2, MOF@DNA1 and **target RNA** were mixed to form a hybrid composite NPMOF@DNA1@**target RNA**@FSN@DNA2. This composite was then separated using a magnet. When there is no **target RNA**, only FSN@DNA2 is extracted, which is inactive. Each of the components MOF@DNA1 and FSN@DNA2 was first, respectively, tested for their efficacy for the photodynamic oxidation of 1,3-diphenylisobenzofuran (DPBF) into 1,2-dibenzoylbenzene and the capacity to be extracted from a solution with a magnet, prior to assembly: capture of **target RNA**.

After separation of the composite was subjected to PDBF, which exhibits an absorption band at 426 nm, as an indicator and monitored by colorimetry. Upon illumination, PCN-224 generates $^1O_2(^1\Delta_g)$ and photo-induced oxidation of PDBF occurs, and the 426 nm signal decreases. The linear relationship between DDE% and the concentration is between 10 and 100 fM at pH 7.4, with a limit of detection of 4.94 fM (DDE% is defined as (initial 426 nm absorbance–absorbance at 426 nm after irradiation)/initial 426 nm absorbance × 100%). This biosensor test takes less than 30 min, which is convenient for applications in clinical settings and hospitals.

### 2.4 Sensors based on photoelectrochemical bioassays

Early detection of the human immunodeficiency virus (HIV) using porous porphyrin-based materials has also been a topic of interest, and accurate and sensitive sensing of specific DNA sequences is an essential trait that such devices should have. Photoelectrochemical DNA bioanalysis emerges as an attractive and modern technique in medicine, where the photocurrent is monitored for any changes upon capture and recognition of a target entity, such as DNA. Photocathode-based DNA bioassays turn out to be a method of choice for their stability.[48] Concurrently, porphyrin-based COFs exhibit electrochemical and optoelectronic properties, large surface area and high porosity, good biocompatibility, chemical stability, and non-interferences, rendering them suitable for the development of COF-based photocathodes in photoelectrochemical bioassays. Luo, Fan and collaborators designed an accurate and sensitive sensor device for HIV DNA using a porphyrin-based COF composite as a photocathode.[49] The concept of fabrication is illustrated in Fig. 10. Briefly, a porous vinyl-functionalized COF (COF-V)

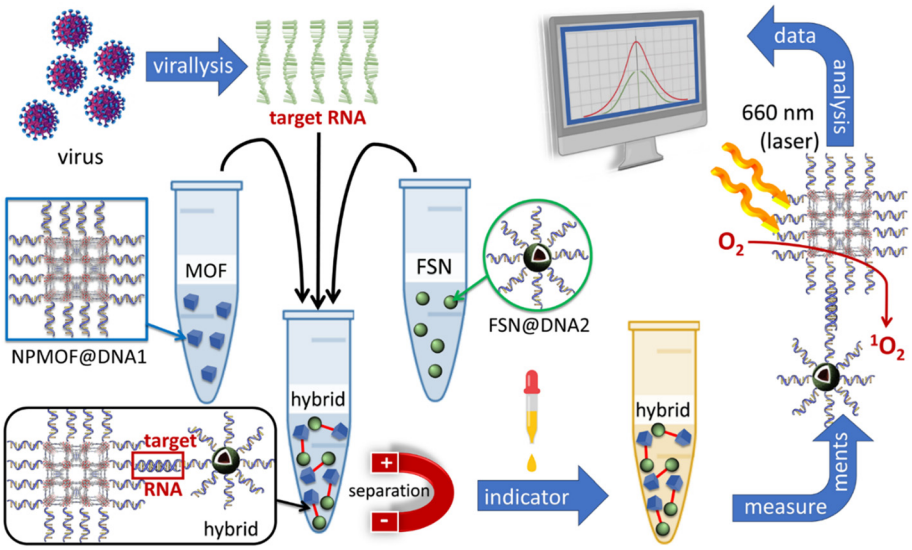


**Fig. 9** Scheme illustrating the multiple step procedure for the detection of RNA related to SARS-CoV-2 based on the photosensitisation of singlet oxygen according to ref. 47. Codes: FSN = FSN@DNA2 = silica-decorated magnetite $Fe_3O_4$@$SiO_2$-$NH_2$@nanoparticles, MOF = composite NPMOF@DNA1, and hybrid = NPMOF@DNA1@**target RNA**@FSN@DNA2.

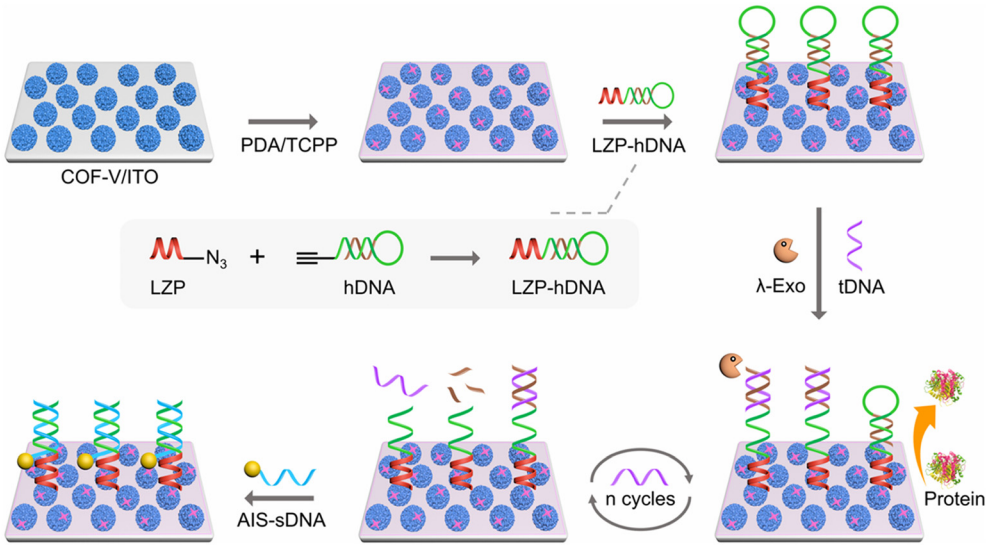


**Fig. 10** Scheme illustrating the construction of the photoelectrochemical DNA bioassay device and the mechanism for the detection of target DNA. The trigger consists in opening the hairpin DNA by the target DNA helped by λ-Exo, which then exposes the attached segment of what is left of the hDNA. Then, the device is prone to recognize and capture the sDNA portion of AIS-sDNA. Reproduced with permission from ref. 49. Copyright ACS 2025.

was first synthesized according to a procedure reported in the literature,[50] which was eventually placed onto indium tin oxide, ITO, a semi-transparent and semiconducting material. These ~300 nm-sized crystalline COF-V spheres (TEM, SEM, XRD) were modified with a *meso*-tetra(4-carboxyphenyl)porphyrin free base ($H_2$TCPP) and polydopamine (PDA), which formed a film upon polymerisation of dopamine, and the nanosphere has a size of ~500 nm (TEM and SEM). This p-type semiconductor, which is part of the photocathode composite PDA/TCPP/COF-V generates a photocurrent that is then used as a transducer.

For recognition purposes, this composite surface was further post-functionalized through strong covalent bonding (*via* Michael or Schiff reactions) with the bioconjugate LZP-hDNA, where LZP is (CPPPPDKDKDKDK-$N_3$), a linear zwitterionic peptide providing a stable anti-interference interface. hDNA is an ethynyl-modified hairpin DNA probe, which covalently binds the azide unit (–$N_3$) of LZP *via* a CLICK reaction. $AgInS_2$ (AIS) nanodots were used as quenchers and were attached to the signaling DNA (sDNA) to prepare the AIS-sDNA labeling. When the target DNA (aided by λ-exonuclease; λ-Exo) was in contact with the bio-modified PDA/TCPP/COF-V photocathode, triggering the chemically induced detection process, a sharp decrease in photocurrent occurred through electron transfer processes across the bio-modified composite. For comparison, the COF-based photocathode response after covalently binding LZP-hDNA onto the surface significantly decreased when the target DNA (10 pM) was added, which decreased a little further when an additional 10 U λ-Exo was co-incubated and decreased even more when AIS-sDNA hybridization was performed onto the bio-surface, signaling total quenching by ~60%. The resulting proximity between the AIS unit and the COF-based photocathode amplifies the quenching process by electron transfer going from the photo-excited AIS unit to the PDA matrix due to the position of their respective valence and conducting bands (Fig. 11b), thus blocking the charge separation process. In the absence of trigger (target DNA), the hairpin DNA does not open and the AIS-sDNA is not captured by the bio-modified surface. The photo-induced formation of hole$^+$-charge$^-$ pairs at the NP interfaces generates ROS type I, leading to the conversion of $O_2$ into $H_2O$ as a result, thus completing the photoelectrochemically driven cycle (Fig. 11a). The linear range is found to be quite large (0.1 fM to 100 pM from the graph of $\Delta I$ *versus* log[conc.], where $\Delta I$ is the change in photocurrent), and the limit of detection is impressively low (0.04 fM). Interference tests indicate that the HIV target DNA is selectively detected over a large series of DNA oligonucleotides (commercially available), including in a mixture. This technique can also serve at detecting various HIV targets, thus rendering it very versatile and applicable in hospitals.

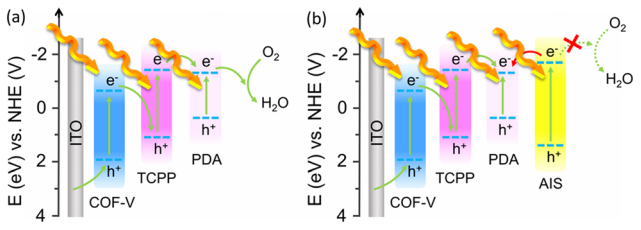


**Fig. 11** Drawing illustrating the photoelectrochemical behaviour at the interfaces of the bio-modified PDA/TCPP/COF-V photocathode in the absence (a) and presence (b) of the target DNA. Reproduced with permission from ref. 49. Copyright ACS 2025.

## Section 3. Antiviral property and photodynamic therapy

The antimicrobial photodynamic therapy, aPDT, is the most efficient manner to control and deactivate viruses. The concept of aPDT using porphyrin-based MOFs and COFs, which focusses mainly on bacteria[51] and fungus so far,[52] is relatively recent but well-known. The technique consists of generating singlet oxygen, $^1O_2(g)$, *in situ* near or on the species to be deactivated. The ground-state electronic configuration of $O_2(g)$ is $(\sigma_s)^2(\sigma_s^*)^2(\sigma_p)^2(\pi)^4(\pi^*)^2(\sigma_p^*)^0$, where the $\pi^*$ manifold is doubly degenerated and leads to three possible electronic states. The first one is the ground state, $^3\sum_g^-$, and the two others are excited states: $^1\Delta_g$ (0.9773 eV) and $^1\sum_g^+$ (1.6268 eV).[53] The direct excitation of molecular oxygen is inefficient as $^3\sum_g^- \rightarrow {}^1\Delta_g$ is spin-forbidden, and consequently, the oscillator strength is small. Alternatively, the photosensitization of singlet oxygen is far more convenient and efficient, and this thermodynamically downhill photophysical event proceeds *via* a collisional process (eqn (1) and Fig. 12):

$$\text{dye}^* + O_2(^3\textstyle\sum_g^-) \rightarrow \text{dye} + O_2(^1\Delta_g) + \text{heat} \quad (1)$$

### 3.1 Production and properties of singlet oxygen

As the photosensitization processes are based on bimolecular collisions, the excited-state lifetimes of the dye* play a crucial role in determining the resulting quantity of produced $^1O_2(^1\Delta_g)$. The longer the excited-state lifetime, the higher the probability of photosensitization. As the triplet ($^3$dye*) lasts significantly longer than the singlet state ($^1$dye*), the latter one is far more inclined to transfer its energy to dioxygen. However, photosensitization from the singlet state also occurs, in parallel.

Concurrently, the other parameter influencing this process is the rate of energy transfer between the dye* and dioxygen.

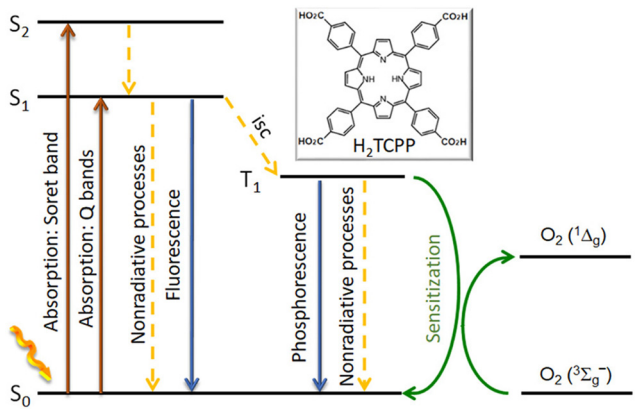


**Fig. 12** Energy diagram of a porphyrin ligand, $H_2TCPP$, as an example, illustrating the unimolecular radiative and nonradiative processes after visible-light irradiation (isc = intersystem crossing) and the sensitization process with molecular oxygen, $O_2(^3\sum_g^-)$. Image reproduced with permission from ref. 51. Copyright ACS 2021.

First, excited-state quenching in the solution is solvent dependent (viscosity and bimolecular interactions). For the management of viruses, water (viscosity is about 1 mPa $s^{-1}$ (Pa = Pascal) or 1 centipoise at 25 °C and about 25% higher for $D_2O$) is the main solvent. So, with such a value of viscosity, if the excited state lifetime of the dye* is shorter than a couple of nanoseconds, then photosensitisation of $^1O_2$ is inefficient or not possible. Another critical aspect is that water also acts as a quencher which deactivates $^1O_2(^1\Delta_g)$. This is well observed from the short-lived excited-state lifetime of $^1O_2(^1\Delta_g)$ ($\tau_{emi}$ is 3.57 μs for $H_2O$ and 77.8 μs for $D_2O$ at 5 °C),[54] which is the shortest one among all other solvents ($3.1 < \tau_{emi} < 994$ μs at room temperature for strongly deactivating solvents, and 7.0 to 463 ms for weakly interacting solvents).[53] Similarly, $H_2O$ has the highest bimolecular quenching rate constant, $k_Q$ ($M^{-1}$ $s^{-1}$) of $^1O_2(^1\sum_g^+)$, in the gas phase.[53] Altogether, the photo-deactivation of viruses in water suffers from the disadvantageous of strong interactions between water and $^1O_2(^1\Delta_g)$, which are likely to be associated with H-bonding. For comparison purposes, the $\tau_P$ value for $^1O_2(^1\Delta_g)$ photosensitized inside the cavities of a porphyrin-based MOF constructed with 5,10,15,20-tetrakis(4-sulfonatophenyl) porphyrin and the oxometallate cluster $[Eu_6(\mu_6\text{-}O)(\mu_3\text{-}OH)_8(H_2O)_{14}]^{8+}$ is 21 ± 1 μs.[55] This longer phosphorescence lifetime, in comparison with $\tau_P$ of 3.1 μs in pure water, is first indicative of strong interactions between $^1O_2(^1\Delta_g)$ and the cavity, which contains multiple $H_2O$ molecules, and also turns out to be convenient for diffusion reasons for antiviral photodynamic therapy actions if the photosensitisation is performed solely in water.

Second, the nature of the dye used also plays a role in the rate of photosensitization of $^1O_2(^1\Delta_g)$. The steric effect is certainly an obvious geometric parameter, which has been demonstrated by different groups.[56] Moreover, upon the bimolecular collision, two energy transfer mechanisms are possible: Forster (intermolecular electric field interactions)[57] and Dexter (double-electron exchange).[58] Their rates of energy transfers ($k_{ET}$) are given by eqn (2) (Forster) and eqn (3) (Dexter):

$$k_{ET} = k_F^\circ(D)\cdot\frac{\kappa^2}{r^6}\cdot\text{cte}\cdot\boldsymbol{J} \quad (2)$$

$$k_{ET} = K\boldsymbol{J}\exp(-2r/L) \quad (3)$$

where $k_F^\circ(D)$ is the radiative rate constant of the energy donor in the absence of energy transfer, $r$ is the center-to-center distance between the donor and the acceptor, cte is $9000\cdot\ln 10/128\ \pi^5\ n^4\ N_a$ (with $n$ being the refractive index of the medium and Na being the Avogadro's number), $L$ is the radius of the energy donor (4.8 Å for porphyrin), and $K$ is a pre-exponential factor. $\kappa^2$ is an orientation factor between the transition moments of the donor and the acceptor, as expressed in eqn (4) (Fig. 13), and $\boldsymbol{J}$ is a normalized integral quantifying the spectral overlap in nm ($\lambda$) between the fluorescence band (or any emission; $F_D$)

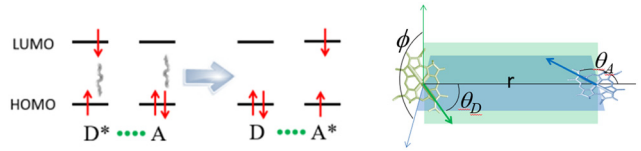


**Fig. 13** (Left) Representation of the electron movements on the frontier molecular orbitals upon electric field interactions between the excited energy donor (D*), also known as the photosensitizer, and the acceptor (A*). The process is D* + A → D + A* + heat. In the Dexter process, the electron of the D* LUMO transfers to the A LUMO while one electron of the A (HOMO) transfers to the D* HOMO. (Right) Schematic of $\theta_D$, $\theta_A$ and $\phi$ in eqn (4), where the green and blue arrows represent the orientation of the transition moment of the electronic transitions involved during the energy process. The images are taken from the SI of ref. 52.

and the absorption band ($\varepsilon_A$) of the energy acceptor, as described in eqn (5):

$$\kappa^2 = (\sin\theta_D \sin\theta_A \cos\phi - 2\cos\theta_D \cos\theta_A)^2 \quad (4)$$

$$J = \frac{\int F_D(\lambda)\varepsilon_A(\lambda)\lambda^4 d\lambda}{\int F_D(\lambda) d\lambda} \quad (5)$$

Because the extinction coefficient is only about 40 to 60 $M^{-1}$ $cm^{-1}$ ($^3O_2(^3\sum_g^-) + h\nu \rightarrow {}^1O_2(^1\Delta_g)$) in organic solvents, it is assumed that it is in the same order of magnitude for water.[59] Then, the *J*-integral is in the lower range (*i.e.* low *J*-integral means slow $k_{ET}$, which means less $^1O_2(^1\Delta_g)$ formed). This explains the often-encountered low phosphorescence intensity of $^1O_2(^1\Delta_g)$ (*i.e.* $^1O_2(^1\Delta_g) \rightarrow {}^3O_2(^3\sum_g^-) + h\nu$). The other parameter included in the *J*-integral is the size of emission band overlap with the absorption of the energy donor. This overlap then becomes extremely variable depending on the spectral position and bandwidth of the dye* emission, which ultimately leads to a high variability of photosensitization efficiencies of the dyes, often referred to as the quantum yield of photosensitization ($\Phi_\Delta$) expressed by eqn (6):

$$\Phi_\Delta = \frac{^1O_2 \text{ produced}}{\text{photons absorbed}} \quad (6)$$

The combination of this situation and the fact that the lifetime of the excited state of the energy donor unavoidably varies leads to a high variability of $\Phi_\Delta$. The extreme cases are that some dyes are simply inefficient at photosensitization. Fortunately, the porphyrin chromophore and its substituted and metallo-derivatives are very good photosensitizers of $^1O_2(^1\Delta_g)$.[60] Moreover, the concentration of $O_2$ in water is about $2 \times 10^4$ M (25 °C), which is relatively large. The combination of these two facts renders the antimicrobial PDT applicable even under aqueous conditions. It is noteworthy that the presence of metallic nodes in MOFs promotes heavy atom effects, thus increasing the rate of intersystem crossing, $k_{isc}$ (Fig. 12), and consequently populating the long-lived triplet state ($T_1$) of the porphyrin chromophore, which then augments the probability of photosensitization.[61,62] Again, this effect depends on the metal size (as the spin–orbit coupling constant increases with the atomic number) and the distance between the chromophore and the heavy atoms. It is also important to note that $k_{isc}$ operates between the $T_1$ and ground state, thus reducing the excited-state lifetime of $T_1$.

### 3.2 Detection of singlet oxygen

As the $\Phi_\Delta$ values are highly variable from one material to another,[62,63] the confirmation of the presence of this ROS is necessary, and absolute quantification of $^1O_2(^1\Delta_g)$ is also possible.[64] Two categories of detection are possible: direct and indirect. The direct detection of $^1O_2(^1\Delta_g)$ can be performed in two manners: electronic paramagnetic spectroscopy (EPR), using a spin trap[65] or not,[66] and emission spectroscopy (*i.e.* $^1O_2(^1\Delta_g) \rightarrow {}^3O_2(^3\sum_g^-) + h\nu$, phosphorescence at ~1270–1280 nm).[52] The detection of diamagnetic $^1O_2(^1\Delta_g)$ (no unpaired electron) by EPR spectroscopy is possible due to the net orbital electronic angular momentum in a magnetic field. In this case, the MO level degeneracy is lifted and then an EPR transition becomes possible. This EPR transition leads to a nearly symmetric quartet (Fig. 14, up left) due to the off-diagonal Zeeman effect. This signal is generally weak since $^1O_2(^1\Delta_g)$ is in the gas phase, short-lived (ms to s) and pressure dependent. However, spin-trapping is favored in solutions, which is in fact an indirect method as well. This technique is generally based on the oxidation of 2,2,6,6-tetramethylpiperidine (TEMP) to 2,2,6,6-tetramethylpiperidine 1-oxyl (TEMPO), which is persistent, using $^1O_2(^1\Delta_g)$. The long stability of TEMPO allows acquiring a high-intensity signal. The triplet of equal intensity is due to spin-nuclei coupling (spin $^{14}N$ = 1).

Concurrently, the direct detection of $^1O_2(^1\Delta_g)$ can be performed by emission spectroscopy where the phosphorescence spectrum of $^1O_2(^1\Delta_g)$ appears at ~1270 to 1280 nm. Typical example of such spectra is shown in Fig. 14(down left),[67] where clear evidence for $^1O_2(^1\Delta_g)$ generation is provided for porphyrin-based MOFs suspended in water and in the solid state, even in porous porphyrin-based coordination networks.[68] The observed differences in the peak maxima (~1270 *vs.* 1280 nm) is due whether $^1O_2(^1\Delta_g)$ is bonded to the metal of the porphyrin or interact somehow with the material (such as H-bonds; 1280 nm), or does not interact at all (~1270 nm).[69] Other indirect methods concern the use of a facile oxidation process of an aromatic compound monitored by either absorption or emission spectroscopy. The two generally used compounds are anthracene and 1,3-diphenylisobenzofuran (DPBF; Fig. 15).[51] The latter is a standard that is commonly used to evaluate $\Phi_\Delta$.

Finally, selective scavengers can be used to react with $^1O_2(^1\Delta_g)$, thus slowing down or stopping its oxidative action towards organic molecules,[70] for instance 9,10-diphenylanthracene or DPBF, during tests. Sodium azide is well-known to quench $^1O_2(^1\Delta_g)$.

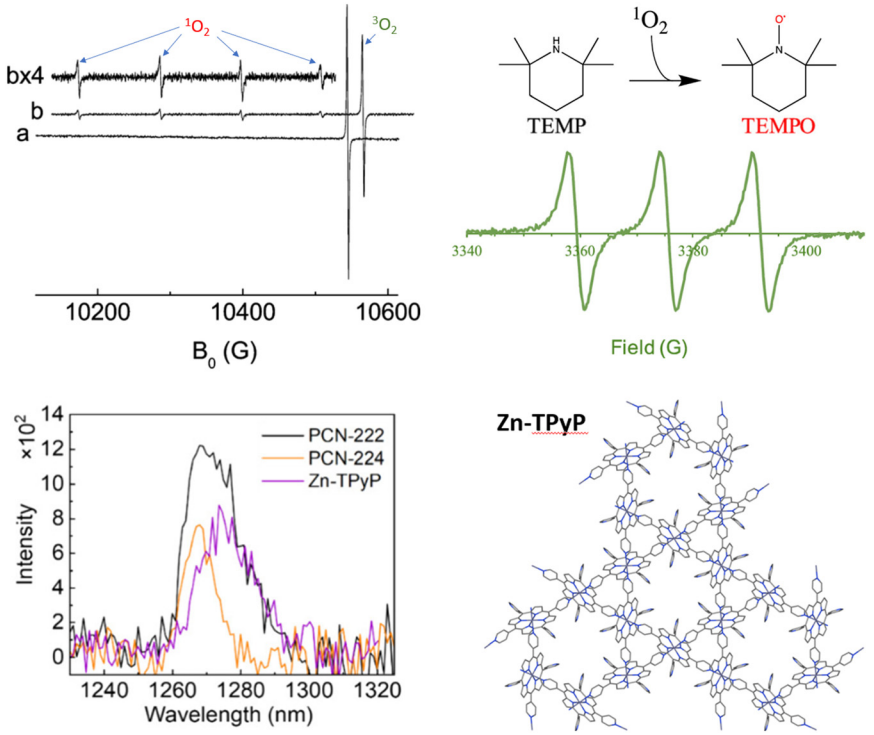


**Fig. 14** (Up left) EPR spectra of $O_2(^3\sum_g^-)$, B = 10 544.68 G ($g$ = 0.6522), where $P_{O2}$= 0.2 Torr: (a) in the dark and (b) with a photosensitizer upon irradiation.[66] (Up right) EPR spectrum of TEMPO when generated by trapping TEMP by $^1O_2(^1\Delta_g)$.[65] This process takes several minutes until stabilisation. Images reproduced with permission from ref. 66 and 65, respectively. Copyright ACS 2013 and ACS 2024. (Bottom) Phosphorescence spectra of $^1O_2(^1\Delta_g)$ photosensitized by PCN-222, PCN-224, and the 3D-porous coordination network [**Zn-TPyP**]$_n$ (its structure is placed beside for convenience; TPyP = tetrakis(pyridyl)porphyrinzinc(II)). The figure showing the spectra (bottom left) is reproduced from ref. 67 and the structure (bottom right) from ref. 68. Copyright ACS 2025 and ACS 2022, respectively.

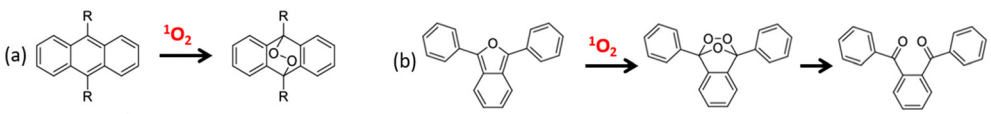


**Fig. 15** Photoinduced oxidation reaction of anthracene (a) and DPBF (b) by $^1O_2(^1\Delta_g)$. R is variable but phenyl is common as 9,10-diphenylanthracene has a fluorescence yield of unity.

### 3.3 Mechanism of action of singlet oxygen

First, $^1O_2(^1\Delta_g)$ is short-lived in water (3.1 μs), but its capacity to oxidize organic materials in water by MOFs is well documented.[71] While this time scale is long enough for diffusion in water based on the viscosity of the liquid, thus allowing for bimolecular oxidation processes with organics, it is still on the very short end of the spectrum. This is where the porosity of the materials come to play. It is known that MOFs are prone to efficiently adsorb molecules at the surface or even inside the pores. This is particularly true when the organic molecules are polar or bear sites for H-bonding. Then once bonded, these species are placed precisely where $^1O_2(^1\Delta_g)$ is photosensitized. This fact has been recently well demonstrated for the degradation of antibiotics at the 100-ppb level using a porphyrin-based MOF, 3D-[$Zn_2$(TPyP)$(NO_2)_2]_n$ (TPyP: 5,10,15,20-tetrapyridylporphyrin), within one hour (Fig. 16).[67] It is worth noting that the ultrafast exciton migration helps to delocalize the absorbed light energy rapidly throughout the materials until photosensitization occurs at the interface of the material. This

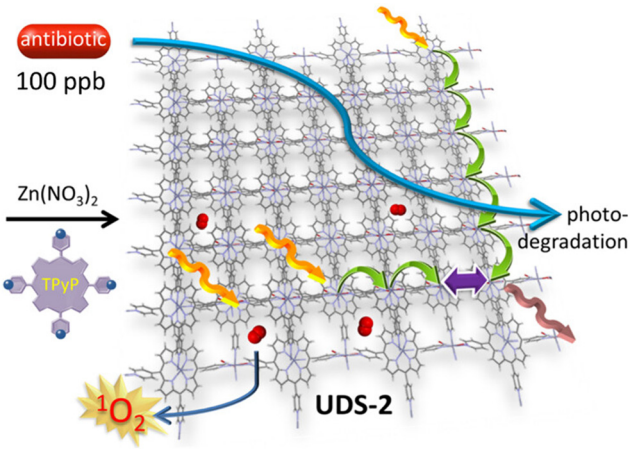


**Fig. 16** Scheme illustrating the photophysical events that occur at the surface of 3D-[$Zn_2$(TPyP)$(NO_2)_2]_n$ (UDS-2), leading to the efficient adsorption and photodegradation of antibiotics by $^1O_2(^1\Delta_g)$. Image reproduced from ref. 67. Copyright ACS 2025.

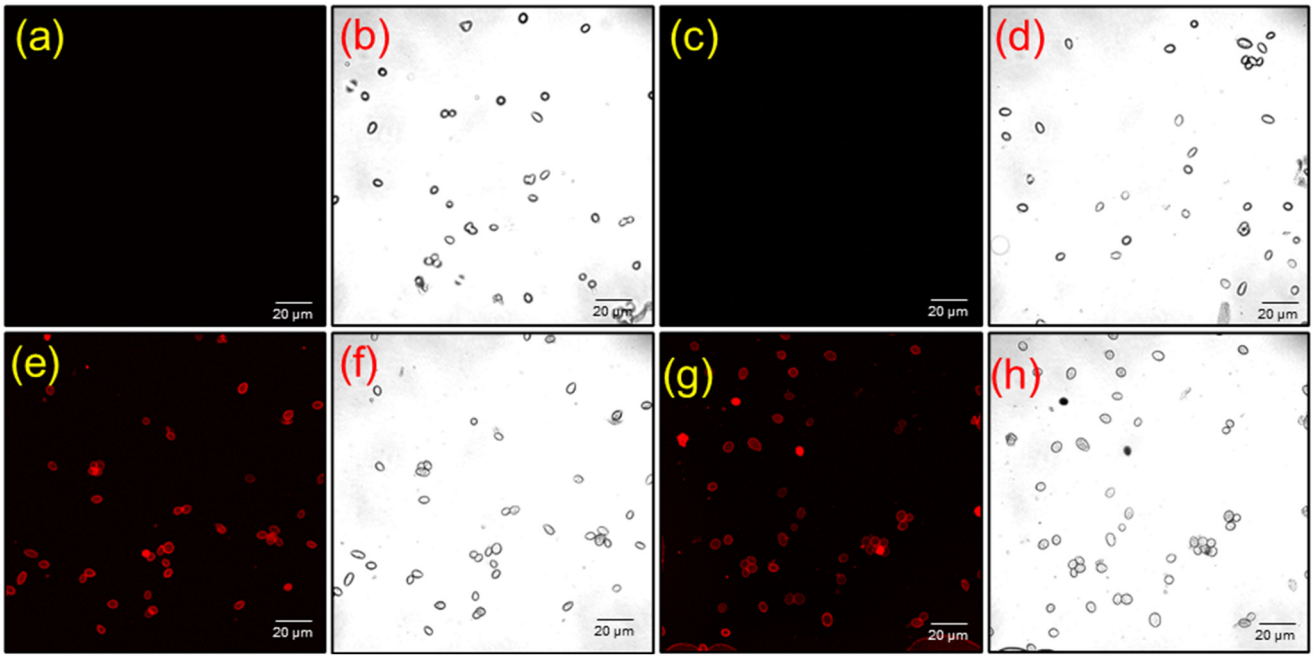


**Fig. 17** *B. cinerea* spores were incubated with various porphyrin-free bases for 1 h, followed by confocal microscopy. Images are shown under illumination by white light (b, d, f and h) or 406 nm (a, c, e and g). Images show spores incubated with nothing (a and b; control), TPP (c and d), TMePPTos (e and f), or TSPPA (g and h). All images were acquired at 40× magnification. Image was reproduced from ref. 72. Copyright ACS 2025.

basic material-related photophysical event contributes significantly to this photosensitization.

Moreover, in a very recent biological *in vivo* and *in vitro* study, stand-alone fluorescent porphyrin free-bases (TMePPTos: 5,10,15,20-(tetra-*N*-methyl-4-pyridyl)porphyrin tetratosylate; TPP: 5,10,15,20-tetraphenylporphyrin; and TSPPA: 5,10,15,20-(tetra-4-sulfonatophenyl)porphyrin tetraammonium) were tested for the photo-eradication of the common fungus *Botrytis cinerea* in tomatoes and apples, using resistant and non-resistant strains.[72] While TMePPTos and TSPPA were efficient at both curing and preventing infections, TPP was inert. The reason is that the ionic species adhere to the cell walls of the *B. cinerea* spores as illustrated in Fig. 17. By confocal microscopy, the fluorescent porphyrins that stuck to the surface of the cell walls were readily detected (red ovals), otherwise no fluorescence was observed, implying that no attachment to the spores occurred and the porphyrin (TPP) was washed away upon rinsing. In brief, the deactivation of viruses involves the adsorption of these viruses onto the surfaces or inside the pores for the porphyrin-based MOFs or COFs, prior to deactivation.

### 3.4 Applications of porphyrin-based MOFs and COFs

Volkringer and his collaborators tested the antiviral performance of PCN-222, PCN-223 and PCN-224 (Fig. 2) and of Al-TCPP (a 2D-nanosheet porphyrin-based MOF), against

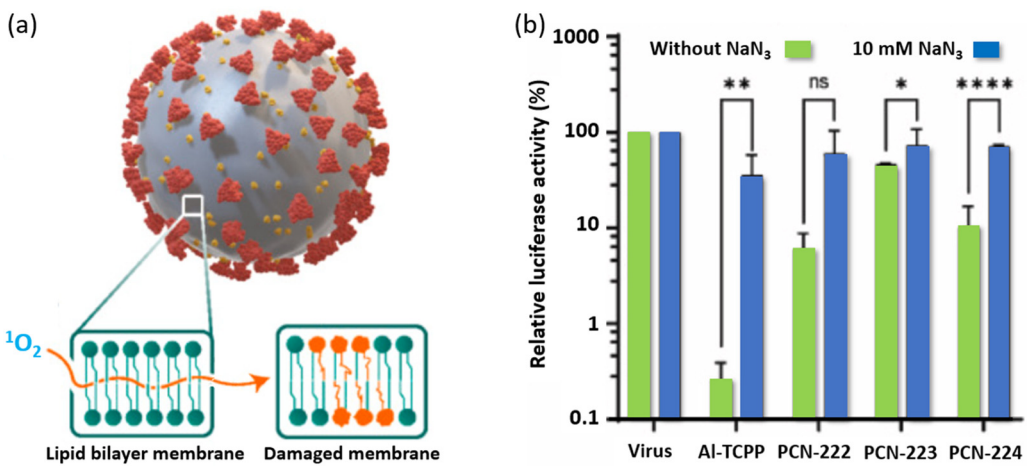


**Fig. 18** (a) Schematic illustrating the mode of action of $^1O_2(^1\Delta_g)$ onto the bilayer membrane of a virus envelope. (b) Relative luciferase activity as a function of the experimental conditions for each porphyrin-based MOF. Reproduced with permission from ref. 73. Copyright Elsevier 2024.

HCoV-229E (SARS-CoV-2 and MERS-CoV) and hepatitis C virus (HCV).[73] The *in vitro* test indicated that Al-TCPP and PCN-222 deactivated HCoV-229E by, respectively, 99.98% and 99.96% when under illumination for 15 min. Similarly, SARS-CoV-2 was photo-deactivated by 99.95% and 93.48%, respectively, for the same irradiation time. Finally, Al-TCPP was tested against MERS-CoV and HCV and the deactivation of MERS-CoV and HCV by, respectively, 99.28% and 98.15%. All four porphyrin-based MOFs photosensitize $^1O_2(^1\Delta_g)$, as established by the effect of sodium azide used as a scavenger. As predicted, the photoproduced $^1O_2(^1\Delta_g)$ oxidizes the phospholipids at the surface of the cell walls (Fig. 18a). One experiment involved monitoring the luciferase activity of HCoV-229E-Luc under various conditions. Luciferase is an enzyme that catalytically oxidizes luciferin and produces bioluminescence. In the absence of porphyrin-based MOFs, no $^1O_2(^1\Delta_g)$ is photosensitized under illumination, and hence, the activity is optimum (Fig. 18b; see the first two bars). In the presence of the MOFs under irradiation, $^1O_2(^1\Delta_g)$ is formed, which causes damages to the virus. This process seriously reduces the luciferase activity (green bars). The best two MOFs are found to be Al-TCPP and PCN-222. Upon adding the $^1O_2(^1\Delta_g)$ scavenger $NaN_3$, the activity is somewhat at the same level as if there was no $^1O_2(^1\Delta_g)$. PCN-223 and PCN-224 appear to be lesser efficient. After a series of antiviral tests against the above-mentioned viruses, it was found that Al-TCPP is the best MOF.

In addition to taking advantage of $^1O_2(^1\Delta_g)$ photosensitisation, other methods which simply involve bringing the viruses to the surface of porphyrin-based MOF NPs or their composite have been developed. For instance, by adding $Mn_3O_4$ NPs, an oxidizing and reducing agent and a catalyst, to a 2D-MOF (Cu-TCPP, Fig. 19a), influenza A virus can be deactivated according to both *in vitro* and *in vivo* tests.[74] Indeed, the half maximal inhibitory concentration (IC50) ranges from 1.21 to 2.39 μg $mL^{-1}$ and from 0.79 to 1.47 μg $mL^{-1}$ for Cu-TCPP and Cu-TCPP@$Mn_3O_4$, respectively, for five strains of influenza A virus: A/Puetro Rico/8/34, A/PR/8/34 with NA-H274Y, A/WSN/1933, A/Aichi/2/68, and A/FM/1/47 (*in vitro* tests and western blotting assay). TEM images showed that the viruses could be adsorbed at the Cu-TCPP surface where evidence for virus envelope disruption was observed. A549 cells (human lung carcinoma cell line) were used for other *in vitro* tests leading to the same observations and corroborative conclusions about the antiviral behavior of Cu-TCPP and Cu-TCPP@$Mn_3O_4$. One important missing information is the mechanism of virus deactivation. *In vivo* tests using mice were also conducted. Overall, this study also reveals that the composite Cu-TCPP@$Mn_3O_4$ binds to the hemagglutinin proteins of the virus envelope, preventing the influenza A virus from penetrating the cellular membrane and preventing the infection of healthy cells (Fig. 19a).

## Section 4. Nanodelivery

When the photo-induced deactivation of viruses by ROS, or blocking access to the viruses to penetrate the walls of healthy cells is not possible, then one can consider drug delivery as an alternative. MOFs in general exhibit another physical feature that is the encapsulation of molecules inside their pores; therefore, their efficiencies and utilities depend on their biocompatibility and capacity of adsorbing the drug molecules and their release rates. In a recent study, particles of micrometer-sized PCN-224 (with 3D-[Zn(2-methylimidazole)$_2$]$_n$, ZIF-8, NPs) were tested against HIV-reservoirs using antiretroviral treatments, which involves delivering drugs capable of blocking one of the various stages of the virus life cycle, thus preventing replication.[75] The

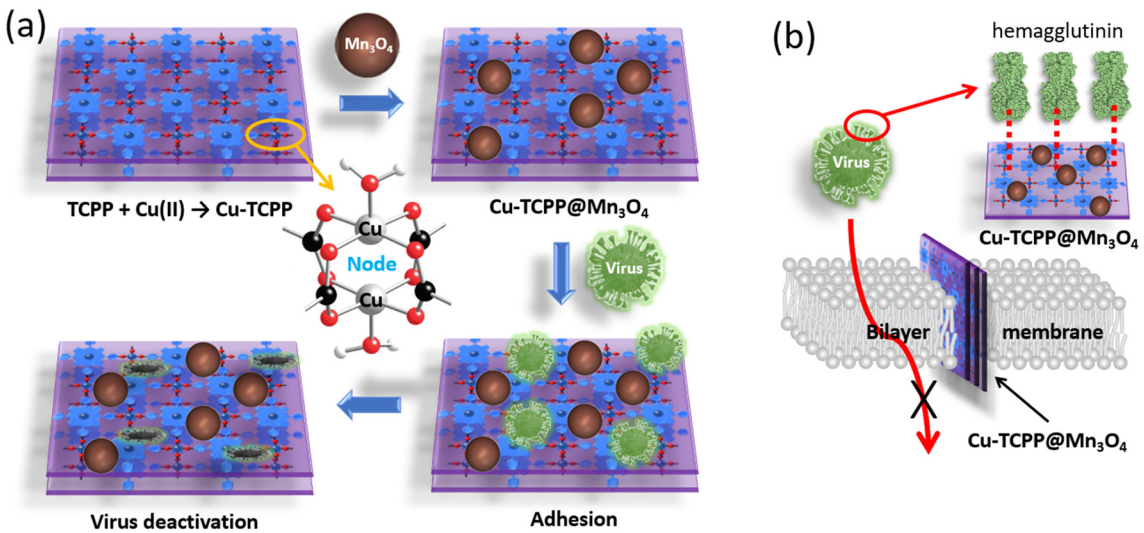


Fig. 19 (a) Illustration showing the preparation of 2D Cu-TCPP and Cu-TCPP@$Mn_3O_4$ and their mode of action for the deactivation of influenza A virus. Note that in the presence of water, the Cu(II) metal is most likely coordinated with $H_2O$ molecules. (b) Illustration showing the mode of action of Cu-TCPP@$Mn_3O_4$ pertaining to its interactions with hemagglutinin, thus preventing viruses from penetrating healthy cells according to ref. 74.

biocompatibility of PCN-224 was demonstrated using the CyQUANT™ lactate hydrogenase assay. It was found that PCN-224 exhibits negligible cytotoxicity at 0–500 μg $mL^{-1}$ in multiple human cell lines. It is noteworthy that due to the strong luminescence of PCN-224, the cytotoxicity assay based on a luminescent probe (epifluorescence microscopy) cannot be applied. In addition, PCN-224 showed no significant *in vitro* hemolytic activity (breakdown of red blood cells) at concentrations lower than 500 μg $mL^{-1}$. Moreover, PCN-224 was tested for platelet aggregation (process that controls the hemostasis), as too much aggregation may lead to thrombotic diseases (a percentage above 60% is a risk factor). The tests show that PCN-224 does not exhibit platelet aggregation within the concentration range of 0–500 μg $mL^{-1}$. The antiretroviral drugs are shown in Fig. 20 (combination 1: emtricitabine/bictegravir/tenofovir, FTC/BIC/TFV; combination 2: nevirapine/tenofovir/emtricitabine, NVP/TFV/FTC). The encapsulation efficiency in percent (% EE = $\{1 - ([drug]_{supernatant}/[drug]_{total})\}$) of PCN-224 of these drugs varies from 68 to 88%, values that are considered high. The release of these drugs followed first-order kinetics, and the rate constants, $k$, obtained from % $drug_{released} = a(1 - \exp(-kt))$, are reported in Fig. 20(right). Interestingly, these rates are found to be combination dependent, suggesting specific interactions with PCN-224. The micrometer size of the PCN-224 particles prevented *in vivo* studies. Conversely, the nanometer-sized ZIF-8 MOF allowed such studies in HeLa cell lines, which showed high cellular uptake.

## Section 5. Photo-sanitary fabrics

When COVID-19 pandemic hit the planet, an urgent need for immediate protection emerged until vaccines were developed, also calling for the rapid modification of ventilation strategies to impede the microbial aerosols,[76] notably for COVID-9 patients. Ultimately, protective nose/mouth masks turned out to be the rapid and handy temporary solution worldwide. However, modified fabrics with anchored porphyrin-based MOF photosensitizers of $^1O_2(^1\Delta_g)$ for self-cleaning[76] and antimicrobial purposes[51] have been developed, which are well-known tactics. It is only recently that the use of 2D-porphyrin-based COFs in fabrics has emerged for photo-sanitary purposes against viruses (see the principle and details in Fig. 21).[77]

The porphyrin-based MOF, DhaTph-COOH, was fully characterized by BET, IR spectroscopy, powder-XRD, TEM, DLS (dynamic light scattering), ICP (inductively coupled plasma) and XPS (X-ray photoelectron spectroscopy), and it was determined that the average particle size was 396 nm and the average pore size was 1.83 nm. The composite, Ag@DhaTph-COOH, was also fully characterized, and the dispersed Ag NPs throughout the COF material exhibited a particle size smaller than 5 nm, indicating that they are placed between layers. The addition of Ag NPs increased the hydrophilicity of the composite, which appears as an extra-convenient feature.

The performance of photosensitization of $^1O_2(^1\Delta_g)$ by Ag@DhaTph-COOH was also assessed using the photooxidation reaction of DPBF (Fig. 15b) irradiated with visible light ($\lambda > 400$ nm (filtered), ~50 mW $cm^2$ at the sample) and showed faster photodegradation of DPBF (within a minute) than that of DhaTph-COOH. Although not specifically specified, the heavy atom effect, which promotes enhanced spin–orbit coupling and faster rates of intersystem crossing, may populate even more the triplet excited state of porphyrins, thus increasing their probability to interact with dioxygen. Further evidence for $^1O_2(^1\Delta_g)$ was provided by EPR spectroscopy using TEMP as a spin-trap (Fig. 14, up right). A concomitant effect is the temperature increase upon illumination ($\Delta T$), which were +14 and +17 °C for DhaTph-COOH and Ag@DhaTph-COOH, respectively. Under sunlight, the composite even showed a variation of +18 °C and remained stable ($41 < T(°C) < 43$) for at least 3 hours. No supplementary test was performed to identify whether other ROS (type I: radicals) and holes were at play.

In addition to the demonstrated good antibacterial behavior of DhaTph-COOH and Ag@DhaTph-COOH against *E. coli* (>97%) and *S. aureus* (>96%), these nanomaterials

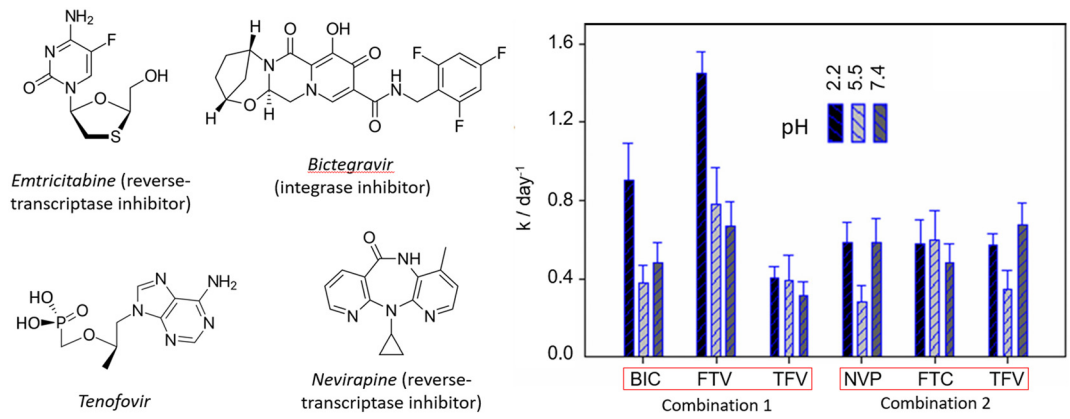


**Fig. 20** Left: molecular structures of the antiretroviral drugs. Right: delivery rate constants of the antiretrovirals at different pH values and combinations by PCN-224. Reproduced with permission from ref. 75. Copyright RSC 2024.

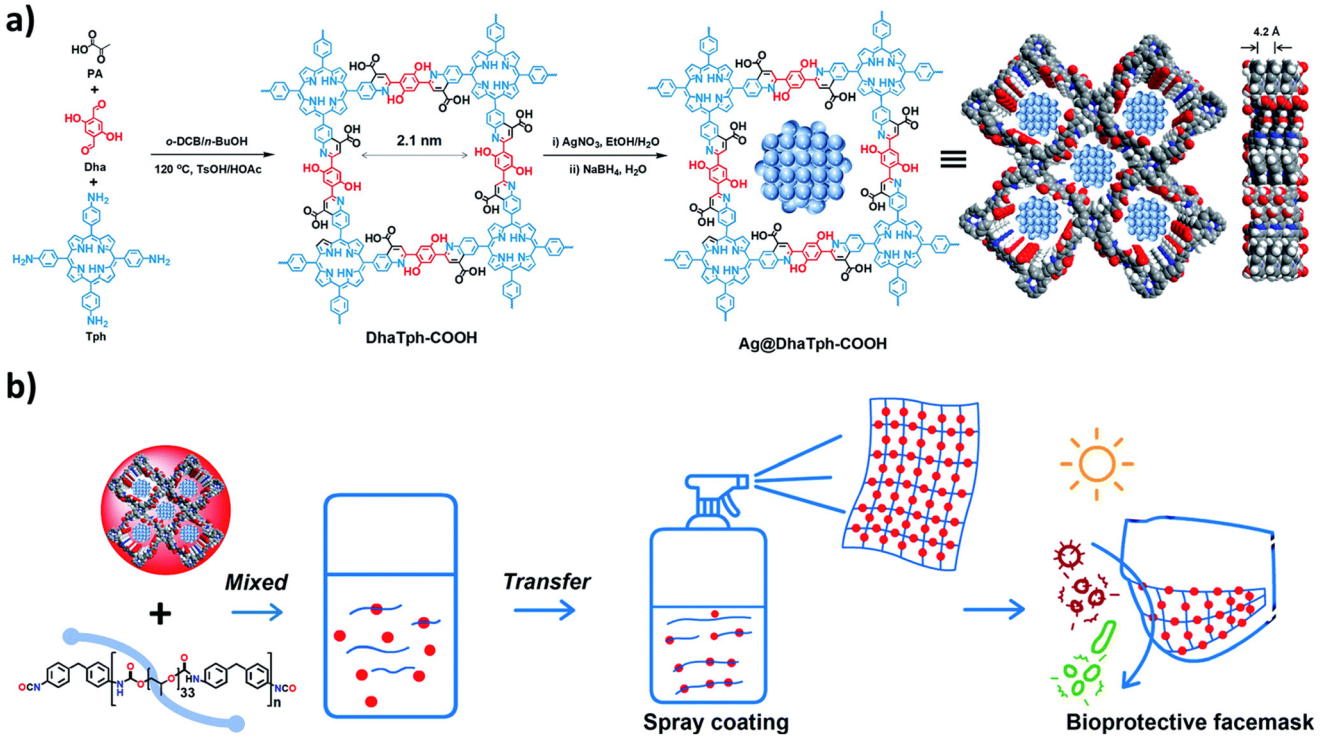


**Fig. 21** (a) Illustration showing the preparation of the porphyrin-based COF composites. First, a three-component one-pot Doebner reaction is performed for COF DhaTph-COOH (note: the $N_2$ adsorption capacity and BET surface area are 259.3 $cm^3\ g^{-1}$ and 306.9 $m^2\ g^{-1}$, respectively). Then, this COF exhibiting an excellent solubility in various organic solvents and water solutions is post-functionalized by Ag NPs, giving the composite Ag@DhaTph-COOH, where the NPs are located within the pores of COFs ($N_2$ adsorption capacity and BET surface area are 224.6 $cm^3\ g^{-1}$ and 259.3 $m^2\ g^{-1}$, respectively). The structure on the right-hand side is a simulation, which exhibits an interlayer separation of 4.2 Å. (b) This composite NP is HO-enriched and then mixed with OCN-terminated polyurethane oligomers in anhydrous $CHCl_3$ to securely and covalently bind the composite NPs to the oligomers. The resulting dispersion was carefully and homogeneously sprayed over a non-woven polyethylene terephthalate fabric, which was then dried (80 °C for 6.0 h). Reproduced with permission from ref. 77. Copyright RSC 2022.

were tested against the vesicular stomatitis virus (VSV) and influenza A virus (A/H1N1) using HeLa and MDCK cell lines, respectively, under visible light ($\lambda > 400$ nm, ~50 mW $cm^2$) and sunlight conditions (50–54 mW $cm^2$), as well as in the dark as controls. Three processes can occur: chemotherapy induced by the Ag NPs, photothermal therapy, and photodynamic therapy, either separately or combined (Fig. 22, top). In the dark, only chemotherapy can occur, and the parameter $TCID_{50}$, the number of infectious viruses expressed as the 50% infective dose in cells, was evaluated and compared to that when irradiated. For example, for VSV *versus* Ag@DhaTph-COOH, quasi-complete inactivation (99%) was achieved in 1 hour. Conversely under the same conditions, DhaTph-COOH deactivates the viruses to a level of ~78%. More specifically, for a sample of VSV ($2 \times 10^7$ $TCID_{50}$/ml; blank), on a log scale, a decrease in $TCID_{50}$ varied from 7.0 to 6.6 to 4.2 for a blank, in the presence of DhaTph-COOH and Ag@DhaTph-COOH, respectively. Under visible light, these values went from 6.2, 3.3 and 1.0, respectively. Finally, under sunlight exposure, quasi-complete deactivation of the virus was observed. The use of the scavenger, $NaN_3$, confirmed the presence of $^1O_2(^1\Delta_g)$. The reusability test showed a quasi-stable performance of Ag@DhaTph-COOH *versus* VSV and A/H1N1 going from 99% (both) to 97 and 96%, respectively (in 5 cycles).

The functionalization of facemasks (details are given in the caption of Fig. 21). The polyurethane hybrid, Ag@DhaTph-COOH@M, was also fully characterized by IR spectroscopy, PXRD, BET, TGA, SEM, and SEM–EDX. The SEM images (Fig. 22, bottom) show that the fibers are well-blended with a dense and homogeneous coating of Ag@DhaTph-COOH (thickness ~ 100 μm). Due to the presence of polyurethane, the hybrid mask is more hydrophobic than that of the stand-alone composite, which conveniently prevents droplets from adsorbing onto the fabric. In addition to antibacterial tests, the bio-protective ability of the modified mask was assessed against A/H1N1-containing aerosols ($1 \times 10^4$ $TCID_{50}$/mL) using a nebulizer (flow rate = 200 mL $min^{-1}$). The self-sterilizing test revealed that after 60 min of irradiation under sunlight conditions, the antiviral efficiencies still reached 99%, and after 5 cycles, this value just dropped to 95%.

## Conclusion

With the aim of managing virus threat, porphyrin-based MOFs and COFs are often solicited. This is rendered possible as these materials are semi-conductors and efficient at photosensitizing $^1O_2(^1\Delta_g)$. In this mini-review, the design of

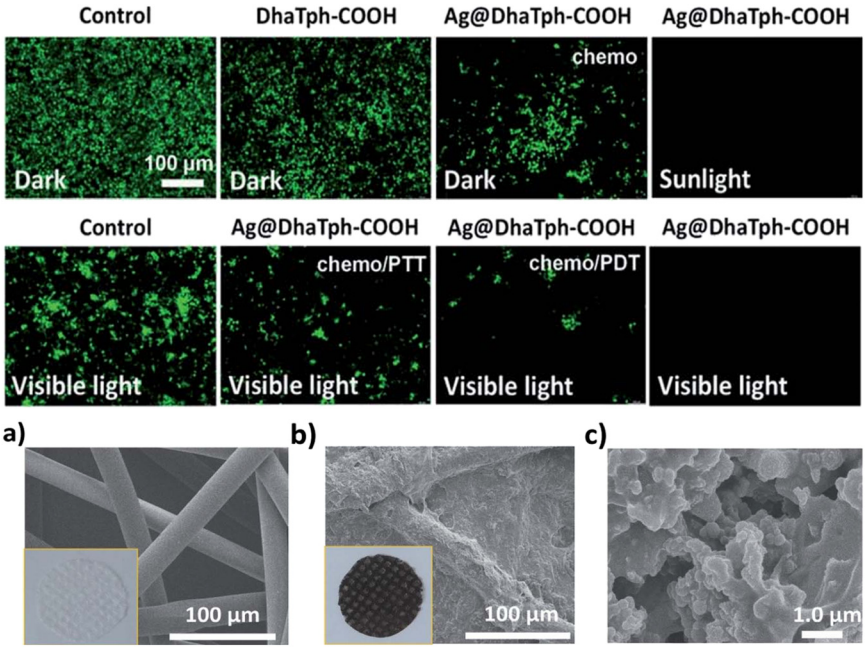


**Fig. 22** Top: immunofluorescence microscopic images of the VSV-infected HeLa cells after treatment under different conditions. (Chemo = chemotherapy induced by the Ag NPs; PTT = photothermal therapy; and PDT = photodynamic therapy, *i.e.* $^1O_2(^1\Delta_g)$). Bottom: (a) SEM image of the facemask cloth. (b) and (c) SEM images of the facemask cloth with the Ag@DhaTph-COOH coating. Reproduced with permission from ref. 77. Copyright RSC 2022.

sensors, protection devices and nanotechnologies against viruses, using porphyrin-based MOFs and COFs, was reported. However, this field of research is found to be still in its infancy in comparison with MOFs and COFs in general. Despite this youth, the current results has already demonstrated quite mature advancements based on performance metrics.

In the area of sensors, which is generally far more developed than that of the inactivation of viruses, modern technics are advantageously exploited, which are largely based on RNA detection as a trigger of a change in an analytical signal. However, there is still room for further developments by taking advantage of other material responses. Recently, surface plasmon resonance (*i.e.* when a polarized light arrives with a specific angle on a thin film, depending on the material, it generates surface plasmon polaritons) has emerged as a powerful modern technique combining rapid responses, non-destructive method, high specificity and sensitivity, real-time on-site detection, and continuous monitoring advantages, which has been recently reviewed.[78] In the area of MOFs, a UiO-66-based device was able to detect single strands associated with SARS-CoV-2 in a linear detection range of 10–400 mg $mL^{-1}$ with a limit of detection of 0.9625 ng $mL^{-1}$. However, this technique experiences some challenges, and further developments are to be expected.

The antiviral approach based on PDT ($^1O_2(^1\Delta_g)$) is mostly an interfacial phenomenon on the NP surfaces due to the relative size of viruses (20–200 nm *versus* porphyrin-based MOF and COF pore sizes, several nanometers) and to the relatively short lifetime of $^1O_2(^1\Delta_g)$ in water (3.1 μs).[53] This ROS is a powerful oxidizing agent that degrades organics efficiently.[78] However, this methodology is limited to only ideal cases where the need for visible light is fulfilled. It is also noteworthy that, despite this limitation, taking into account the large library of possible viruses and porphyrin-based MOFs and COFs, further extensive developments are expected. When the medium prevents light from penetrating efficiently into the matrix (for instance, flesh or the virus foyer), drug delivery is a possible alternative.[75] The pore sizes of porphyrin-based MOFs and COFs are sufficiently large enough for numerous medicinal molecules to be incorporated inside these nanocarriers.

In the field of self-sanitary fabrics, the clever use of a COF composite and a hybrid was presented and briefly described. Concurrently, porphyrin-based MOFs could also be employed since examples such as PCN-222 and PCN-224 have demonstrated no or negligible cytotoxicity (Fig. 3),[9] and fabrics based on covalently attached Zr(IV)/porphyrin-based MOFs can also be expected. The efficiency to photosensitize $^1O_2(^1\Delta_g)$ (often called the singlet oxygen quantum yield) and other ROS is also MOF dependent.

Furthermore, the recent review on MOFs in general (in which porphyrin-based MOFs and COFs were absent due to lack of development at that time of publication), demonstrated that the 6 modes of action for virus managements exist (physical barrier, encapsulation, mineralisation, antiviral based on contacts, photosensitization, and drug delivery).[1] In this present review on porphyrin-based porous materials, encapsulation and mineralisation strategies are absent. One of

the reasons is that the encapsulation of a virus requires the rare combination of a very small virus and mesoporous materials, which very rarely exist in porphyrin-based MOFs and COFs. Similarly, the mineralisation process cannot be easily applied when the syntheses of these nanomaterials do not occur spontaneously. Instead, harsh conditions need to be applied to prepare these materials (for example solvothermal reactions). Consequently, no development is expected in the near future using these NPs.

Finally, with regard to the wealth of reported photocatalysis applications of porphyrin-based MOFs and COFs in the fields of eradication of bacteria,[51] cancer therapies,[78] reduction of high-valent toxic metals in contaminated water,[70,79] agricultural management,[39] degradations of toxins and organic pollutants in used water,[80] organic synthesis[81] and generation of solar fuels,[82] this review on viruses differs profoundly. While all previous applications rely on effortless adsorptions of species either onto the surface on inside the pores of the NPs, the efficient capture of viral RNA for stimulus-driven detection purposes requires a quite complex device fabrication strategy (Fig. 5–10). Similarly, the desired efficient interactions between the virus hemagglutinin proteins and the nano-NPs for antimicrobial PDT are not automatic. There is a need for appropriate biological ingredients or conditions for this purpose. Therefore, without surprise, the late occurrence of emerging technologies in this field with respect to the above-mentioned applications is simply due to its inherent bio-complexity.

## Conflicts of interest

There are no conflicts of interest to declare.

## Data availability

No primary research results, software or code have been included and no new data were generated or analysed as part of this review.

## Acknowledgements

P. D. H. acknowledges the Natural Sciences and Engineering Research Council (NSERC) of Canada for the financial support (#RGPIN-2019-05289).

## References

1 L. Boivin and P. D. Harvey, *ACS Appl. Mater. Interfaces*, 2023, **15**(11), 13844–13859.
2 G. da Rosa, P. H. H. Silva, J. V. J. Silva Júnior, M. M. Pillat, B. A. Iglesias, R. Weiblen and E. F. Flores, *Antiviral Res.*, 2025, **243**, 106279.
3 S. Choi, S. Kulkarni, E. Arnett, L. S. Schlesinger, B. E. Britigan and P. Narayanasamy, *ACS Infect. Dis.*, 2024, **10**, 4279–4290.
4 Z. A. Arnaut, S. M. A. Pinto, R. T. Aroso, A. S. Amorim, C. S. Lobo, F. A. Schaberle, D. Pereira, J. Núñez, S. C. C. Nunes, A. A. C. C. Pais, P. Rodrigues-Santos, L. P. de Almeida, M. M. Pereira and L. G. Arnaut, *Photochem. Photobiol. Sci.*, 2023, **22**, 2607–2620.
5 Y. A. Gubarev, N. Sh. Lebedeva, E. S. Yurina, G. M. Mamardashvili, S. V. Zaitceva, S. A. Zdanovich and O. I. Koifman, *J. Biomol. Struct. Dyn.*, 2022, 1–10.
6 K. Vashishtha, F. Xi, P. Dharmalingam and A. Douplik, *Appl. Sci.*, 2023, **13**, 1426.
7 R. Rathnasinghe, S. Jangra, L. Miorin, M. Schotsaert, C. Yahnke and A. García-Sastre, *Sci. Rep.*, 2021, **11**, 19470.
8 S. Jeoung, S. Kim, M. Kim and H. R. Moon, *Coord. Chem. Rev.*, 2020, **420**, 213377.
9 F. Hao, Z.-Y. Yan and X.-P. Yan, *Sci. Total Environ.*, 2022, **833**, 155309.
10 H. F. Blum and C. R. Spealman, *Am. J. Physiol.*, 1934, **109**, 605–613.
11 F. Kradolfer and R. Wyler, *Z. Hyg. Infektionskrankh.*, 1957, **143**, 416–428.
12 R. Braun and F. Kradolfer, *Phytopathol. Z.*, 1961, **41**, 247–264.
13 B. R. Munson and R. J. Fiel, *Res. Commun. Chem. Pathol. Pharmacol.*, 1977, **16**, 175–178.
14 A. A. Lewin, L. E. Schnipper and C. S. Crumpacker, *Exp. Biol. Med.*, 1980, **163**, 81–90.
15 L. E. Schnipper, A. A. Lewin, M. Swartz and C. S. Crumpacker, *J. Clin. Invest.*, 1980, **65**, 432–438.
16 M. Perlin, J. C. H. Mao, E. R. Otis, N. L. Shipkowitz and R. G. Duff, *Antiviral Res.*, 1987, **7**, 43–51.
17 R. Pompei, G. Cisani, G. Foddis and M. A. Marcialis, *Microbios*, 1989, **58**, 101–111.
18 A. P. Savitskii, A. I. Turkin, E. V. Turkina, T. V. Cherednikova, G. V. Ponomarev and B. F. Poglazov, *Dokl. Akad. Nauk SSSR*, 1989, **304**, 1258–1261.
19 R. Pompei, A. Ingianni, G. Foddis and G. Cisani, *Microbios Lett.*, 1989, **40**, 19–23.
20 K. T. Yue, M. Lin, T. A. Gray and L. G. Marzilli, *Inorg. Chem.*, 1991, **30**, 3214–3222.
21 J. L. Matthews, F. Sogandares-Bernal, M. Judy, K. Gulliya, J. Newman, T. Chanh and A. Marengo-Rowe, *Blood Cells*, 1992, **18**, 75–88, discussion 88-9.
22 A. R. Neurath, N. Strick, P. Haberfield and S. Jiang, *Antiviral Chem. Chemother.*, 1992, **3**, 55–63.
23 D. L. DeCamp, L. M. Babe, R. Salto, J. L. Lucich, M. S. Koo, S. B. Kahl and C. S. Craik, *J. Med. Chem.*, 1992, **35**, 3426–3428.
24 D. W. Dixon, M. S. Kim, V. Kumar, G. Obara, L. G. Marzilli and R. F. Schinazi, *Antiviral Chem. Chemother.*, 1992, **3**, 279–282.
25 J. North, S. Freeman, J. Overbaugh, J. Levy and R. Lansman, *Transfusion*, 1992, **32**, 121–128.
26 J. North, H. Neyndorff, D. King and J. G. Levy, *Blood Cells*, 1992, **18**, 129–139, discussion 139-40.
27 P. Meissner, P. Adams and R. Kirsch, *J. Clin. Invest.*, 1993, **91**, 1436–1444.
28 Z. Malik, H. Ladan, Y. Nitzan and Z. Smetana, Antimicrobial and antiviral activity of porphyrin photosensitization, *Proceedings of*

*SPIE-The International Society for Optical Engineering*, ed. G. Jori, J. Moan and W. M. Star, 1994, vol. 2078, pp. 305–312.
29 V. A. Svyatchenko, S. D. Nikonov, A. P. Mayorov, M. L. Gelfond and V. B. Loktev, *Photodiagn. Photodyn. Ther.*, 2021, **33**, 102112.
30 N. Sh. Lebedeva, Y. A. Gubarev, M. O. Koifman and O. I. Koifman, *Molecules*, 2020, **25**, 4368.
31 I. O. Savelyeva, K. A. Zhdanova, M. A. Gradova, O. V. Gradov and N. A. Bragina, *Curr. Issues Mol. Biol.*, 2023, **45**, 9793–9822.
32 M. Cossu, L. Ledda and A. Cossu, *Food Res. Int.*, 2021, **144**, 110358.
33 R.-M. Ion, *Coatings*, 2021, **11**, 393.
34 S. Mehrzad Sajjadinezhad, L. Boivin, K. Bouarab and P. D. Harvey, *Coord. Chem. Rev.*, 2024, **510**, 215794.
35 C. Liu, T. Wang, J. Ji, C. Wang, H. Wang, P. Jin, W. Zhou and J. Jiang, *J. Mater. Chem. C*, 2019, **7**, 10240–10246.
36 D. Hanke, A. Pohlmann, C. Sauter-Louis, D. Höper, J. Stadler, M. Ritzmann, A. Steinrigl, B.-A. Schwarz, V. Akimkin, R. Fux, S. Blome and M. Beer, *Viruses*, 2017, **9**, 177.
37 J. Ma, W. Wang, Y. Li, Z. Lu, X. Tan and H. Han, *Anal. Chem.*, 2021, **93**, 2090–2096.
38 R. Heidari, J. Rashidiani, M. Abkar, R. A. Taheri, M. M. Moghaddam, S. A. Mirhosseini, R. Seidmoradi, M. R. Nourani, M. Mahboobi, A. H. Keihan and H. Kooshki, *Biosens. Bioelectron.*, 2019, **126**, 7–14.
39 S. M. Sajjadinezhad, K. Tanner and P. D. Harvey, *J. Mater. Chem. B*, 2022, **10**, 9054–9080.
40 X. Yang, Y.-Q. Yu, L.-Z. Peng, Y.-M. Lei, Y.-Q. Chai, R. Yuan and Y. Zhuo, *Anal. Chem.*, 2018, **90**, 3995–4002.
41 D. Wu, W. Dong, T. Yin, G. Jie and H. Zhou, *Sens. Actuators, B*, 2022, **372**, 132659.
42 D. Wang, J. Wang, D. Liu, J. He, M. Wang, H. Huang, G. Nie, H. Ding and X. Yan, *Nano Res.*, 2024, **17**, 1827–1836.
43 S. S. Soldan and P. M. Lieberman, *Nat. Rev. Microbiol.*, 2023, **21**, 51–64.
44 Q. L. You, S. K. Ni and L. K. C. Melvin, *Cancer Biol. Med.*, 2018, **15**, 1.
45 D. Wang, J. Wang, X. J. Gao, H. Ding, M. Yang, Z. He, J. Xie, Z. Zhang, H. Huang, G. Nie, X. Yan and K. Fan, *Adv. Mater.*, 2024, **36**, 2310033.
46 G. Mansueto, M. Niola and C. Napoli, *Pathol., Res. Pract.*, 2020, **216**, 153086.
47 Y. Wang, J. Chen, C. Wu and Y. Zhu, *Sens. Actuators, B*, 2024, **406**, 135413.
48 Y.-T. Xu, S.-Y. Yu, Y.-C. Zhu, G.-C. Fan, D.-M. Han, P. Qu and W.-W. Zhao, *TrAC, Trends Anal. Chem.*, 2019, **114**, 81–88.
49 H. Chen, Z. Wang, Y. Zhao, Z.-L. Song, G.-C. Fan and X. Luo, *ACS Sens.*, 2025, **10**, 507–516.
50 M. Wang, Y. Pan, S. Wu, Z. Sun, L. Wang, J. Yang, Y. Yin and G. Li, *Biosens. Bioelectron.*, 2020, **169**, 112638.
51 A. Schlachter, P. Asselin and P. D. Harvey, *ACS Appl. Mater. Interfaces*, 2021, **13**, 26651–26672.
52 O. Boudreau, P. Asselin, S. M. Sajjadinezhad, P. Karsenti, P. Moffett, K. Bouarab and P. D. Harvey, *Adv. Mater. Interfaces*, 2021, **13**, 26651–26672.
53 C. Schweitzer and R. Schmidt, *Chem. Rev.*, 2003, **103**, 1685–1758.
54 M. Bregnhøj, M. Westberg, F. Jensen and P. R. Ogilby, *Phys. Chem. Chem. Phys.*, 2016, **18**, 22946–22961.
55 J. Demel, P. Kubát, F. Millange, J. Marrot, I. Císařová and K. Lang, *Inorg. Chem.*, 2013, **52**, 2779–2786.
56 S. Faure, C. Stern, R. Guilard and P. D. Harvey, *Inorg. Chem.*, 2005, **44**, 9232–9241.
57 T. Förster, *Ann. Phys.*, 1948, **2**, 55–75.
58 D. L. Dexter, *J. Chem. Phys.*, 1953, **21**, 836–850.
59 D. Weldon and P. R. Ogilby, *J. Am. Chem. Soc.*, 1998, **120**, 12978–12979.
60 J. M. Dąbrowski, B. Pucelik, A. Regiel-Futyra, M. Brindell, O. Mazuryk, A. Kyzioł, G. Stochel, W. Macyk and L. G. Arnaut, *Coord. Chem. Rev.*, 2016, **325**, 67–101.
61 L. Zhang, J. Lei, F. Ma, P. Ling, J. Liu and H. Ju, *Chem. Commun.*, 2015, **51**, 10831–10834.
62 C. T. Buru, M. B. Majewski, A. J. Howarth, R. H. Lavroff, C.-W. Kung, A. W. Peters, S. Goswami and O. K. Farha, *ACS Appl. Mater. Interfaces*, 2018, **10**, 23802–23806.
63 Z. W. Jiang, Y. C. Zou, T. T. Zhao, S. J. Zhen, Y. F. Li and C. Z. Huang, *Angew. Chem., Int. Ed.*, 2020, **59**, 3300–3306.
64 Y. Hao, B. M. Liu, T. F. Bennett, C. G. Monsour, M. Selke and Y. Liu, *J. Phys. Chem. C*, 2021, **125**, 7392–7400.
65 C. J. Steen, J. Niklas, O. G. Poluektov, R. D. Schaller, G. R. Fleming and L. M. Utschig, *Biochemistry*, 2024, **63**, 1214–1224.
66 M. Ruzzi, E. Sartori, A. Moscatelli, I. V. Khudyakov and N. J. Turro, *J. Phys. Chem. A*, 2013, **117**, 5232–5240.
67 B. Salahshournia, A. Noroozi, D. Fortin, L. Shkreta, B. Chabot, A. Soldera, H. Cabana and P. D. Harvey, *ACS Appl. Opt. Mater.*, 2025, **3**, 1254–1267.
68 P. Asselin, A. Schlachter, D. Fortin, P.-L. Karsenti and P. D. Harvey, *Chem. Mater.*, 2022, **34**, 7242–7255.
69 P. Asselin, A. Schlachter and P. D. Harvey, *Chem. Commun.*, 2024, **60**, 8692–8695.
70 J. Wang and S. Wang, *Chem. Eng. J.*, 2020, **401**, 126158.
71 P. D. Harvey, *Sep. Purif. Technol.*, 2023, **322**, 124214.
72 S. M. Sajjadinezhad, Z. Goudreau, F. Rivard, M. R. Gonzalez-Lamothe, B. Habermeyer, P. Moffett, K. Bouarab and P. D. Harvey, *ACS Agric. Sci. Technol.*, 2026, **6**(1), 92–102.
73 O.-E. Plastiras, P. Bouquet, I. Raczkiewicz, S. Belouzard, E. Martin De Fourchambault, J. Dhainaut, J.-P. Dacquin, A. Goffard and C. Volkringer, *Mater. Today Bio*, 2024, **28**, 101165.
74 L. Chen, Y. Zou, R. Li, X. Zhou, Y. Lai, J. Chen and J. Yang, *Small*, 2024, **20**, 2306095.
75 J. A. Lebrón, F. J. Ostos, M. Martínez-Santa, F. García-Moscoso, M. López-López, M. L. Moyá, E. Bernal, S. Bachiller, G. González-Ulloa, D. Rodríguez-Lucena, T. Lopes-Costa, R. Fernández-Torres, E. Ruiz-Mateos, J. M. Pedrosa, M. Rafii-El-Idrissi Benhnia and P. López-Cornejo, *J. Mater. Chem. B*, 2024, **12**, 5220–5237.
76 S. Naaz, E. Ozair, A. Asghar, N. Sahay and R. Kumar, *J. Clin. Diagn. Res.*, 2021, **15**, 1–5.
77 L.-G. Ding, S. Wang, B.-J. Yao, W.-X. Wu, J.-L. Kan, Y. Liu, J. Wu and Y.-B. Dong, *J. Mater. Chem. A*, 2022, **10**, 3346–3358.

78 C. Guo, Z. Liu, Y. He, S. Zhang, L. He, M. Wang and Z. Zhang, *Talanta*, 2025, **292**, 128008.
79 P. D. Harvey and J. Porphyr, *Phthalocyanines*, 2023, **27**, 1015–1027.
80 P. D. Harvey and J. Porphyr, *Phthalocyanines*, 2021, **25**, 583–604.
81 P. D. Harvey, *J. Mater. Chem. C*, 2021, **9**, 16885–16910.
82 P. Asselin and P. D. Harvey, *ACS Appl. Nano Mater.*, 2022, **5**, 6055–6082.